EXIT DOSE MEASUREMENT FOR PATIENT TREATMENT DOSE VERIFICATION IN Co-60 TELETHERAPY

A THESIS PRESENTED TO THE

DEPARTMENT OF MEDICAL PHYSICS

SCHOOL OF NUCLEAR AND ALLIED SCIENCES

UNIVERSITY OF GHANA

BY

ABAITEY ABRAHAM BINADEO

10598721

IN PARTIAL FULFILMENT OF THE REQUIREMENTS FOR THE AWARD OF

MASTER OF PHILOSOPHY DEGREE

IN

MEDICAL PHYSICS

JULY,2018

DECLARATION

Student's Declaration:

I hereby declare that, with the exception of references to other people's work which have been duly acknowledged, this work is the result of my own research undertaken under supervision, and neither in whole nor in part has been presented for any other degree at another university elsewhere.

……..... ……...……

Abaitey Abraham Binadeo **Date**

(Student)

…… ……..

Prof. John Humphrey Amuasi **Date**

(Principal Supervisor)

…… ……

Mr. E.K.T Addison **Date**

(Co-Supervisor)

…….. ……

Mr. E.K Sosu **Date**

(Co-supervisor)

ABSTRACT

This work evaluates the possibility of creating an online patient dose verification system through exit dose measurement on a Co-60 teletherapy machine which lacks an electronic portal imaging device (EPID). Exit dose measurements were done by diode and Barracuda and compared to those of an ionization chamber. The diode was first calibrated and the necessary correction factors (depth and field size corrections) determined using a PMMA phantom. The transmission factor of the couch was also determined at gantry angles relevant to the study (0^o and 180^o) and at various field sizes. The estimated couch transmission factor was 0.96912. The exit dose measurements were done both with PMMA phantom and an anthropomorphic phantom by calculating a dose of 200 cGy to the various depths and corresponding field sizes. The detectors were placed 30 cm underneath the treatment couch for all the measurements. Readings from both detectors compared well with those of the ionization chamber. The percentage deviations were generally lower with the PMMA phantom than for the anthropomorphic phantom though they were all below 2%. The diode deviations range between 0.098 to -1.322 for measurements with PMMA phantom at a depth of 15 cm while those of the Barracuda were between 0.157 and -1.411 at the same conditions.

Diode in vivo dosimetry was found to be suitable for the verification of patient dose through exit dose measurements. However the calibration and correction factors must be determined carefully in order to generate more accurate results.

DEDICATION

This work is a special dedication to my parents Mr. Ishmael Abaitey Binadeo and Mad. Janet Danlogo and their grandchildren Evelyn Wekia Awozare, Gerald Jnr Weperi Awozare and Abaiki Dede Binadeo.

ACKNOWLEDGEMENT

I am very thankful to the almighty God for the blessings of wisdom, understanding, good health and resilience throughout the period of this work.

I want to as well extend my sincere gratitude to my supervisors, Prof J. H Amuasi, Mr E. K. T Addison and Mr E. K Sosu for their unrelenting support and encouragement at the times when I could not see any light and all hope was lost. But for their corrections and constructive criticisms this work would not have been possible.

Finally, I acknowledge the prayers, love, support and encouragement to my parents and siblings, friends and loved ones which kept me going from the starting to the finishing of this study

TABLE OF CONTENTS

LIST OF FIGURES

LIST OF TABLES

ABBREVIATIONS

2D	Two Dimensional
3D	Three Dimensional
ALARA	As Low As Reasonably Achievable
CCD	Charge Coupled Device
CR	Computed Radiography
CT	Computed Tomography
CTDI	Computed Tomography Dose Index
EBRT	External Beam Radiotherapy
EPID	Electronic Portal Imaging Device
HVL	Half Value Layer
IAEA	International Atomic Energy Agency
ICRP	International Commission on Radiological Protection
ICRU	International Commission on Radiation Units and Measurements
IGRT	Image Guided Radiotherapy
IMRT	Intensity Modulated Radiotherapy
IORT	Intra-operative radiotherapy
IVD	In Vivo Dosimetry
KATH	Konfo Anokye Teaching Hospital
LINAC	Linear Accelerator

MLC	Multi-leaf Collimator
MOSFET	Metal Oxide Stimulated Field Effect Transistor
MPD	Multi-Purpose Detector
MRI	Magnetic Resonance Imaging
MU	Monitor Units
MV	Megavolts
OSLD	Optically Stimulated Luminescent Dosimeter
PET	Positron Emission Tomography
PMMA	Polymethyl Methacrylate
PSDL	Primary Standard Dosimetric Laboratory
PTV	Planning Target Volume
QA	Quality Assurance
RT	Radiotherapy
RTD	Real Time Display
SABR	Stereotactic Ablative Body Radiotherapy
SLIC	Scanning Liquid-filled Ionization Chamber
SSD	Source to skin distance
TBI	Total body irradiation
TF	Transmission Factor
TPS	Treatment Planning System

VMAT	Volumetric Modulated Arc Therapy
WET	Water Equivalent Thickness

CHAPTER ONE

1.0 INTRODUCTION

1.1 Background

Radiotherapy has become one of the most widely used treatment option, accounting for 80% of cancer treatments complimentary to surgery, chemotherapy, hormonal therapy or immunotherapy. Radiation therapy is delivered in two main forms namely brachytherapy (Curietherapy) and external beam therapy (Teletherapy). Whiles brachytherapy involves the placement of sealed sources (eg Ir-192, Cs-137, Co-60, Au-198, I-125) of radiation close to the target or patient by means of special applicators, teletherapy delivers the radiation from a distant source (Co-60 source unit or a linear accelerator) far from the target or patient (Leite et al., 2013)

The ultimate aim of radiotherapy is to deliver as much conformal radiation dose to the target volume while putting efforts to deliver doses as low as reasonably achievable to the healthy tissue surrounding organs. Efforts to achieving this have improved over the decades with the introduction of complex treatment techniques and imaging modalities such as conformal therapy, fractionation, intensity modulated radiation therapy (IMRT), image guided radiation therapy (IGRT), volumetric modulated arc therapy (VMAT), radiosurgery, image based dosimetric procedures (EPID based in vivo dosimetry) as well as computed tomography (CT), magnetic resonance imaging (MRI), positron emission tomography (PET), single photon emission computed tomography (SPECT) and ultrasonic scans coupled with multitasking treatment planning systems to match. All these are tailored towards reducing the incidence of errors in the entire treatment procedure.

While the imaging modalities complimentarily give a clearer visualization of the target, the conformal technique provides a geometric sparing of the healthy tissues. The modern linear accelerators make use of multileaf (typically 120 individual leaves) collimators (MLC) which are programed and moved independently creating fields of diverse shapes and can be incorporated into the treatment planning system. Fractionation demands a total prescribed of say 70Gy be delivered in 35 sessions of 2Gy each over a longer period of time instead of administering the 70Gy at once. This takes advantage of the radiobiological differences between normal tissues and the cancer cells (early responding) by allowing a relatively rapid sub lethal damage repair in the normal cells while reoxygenation occurs in the tumor cells which is a therapeutic advantage at low doses.(Tan, 2016)

The inhomogeneous beam fluence of the IMRT inverse planning technique allows for even more beam shaping (defined by the MLC) leading to better sparing of organs at risk. This highly advanced photon beam technique delivers radiation of varying intensities to the tumor from several directions and this increases the normal tissue volume irradiated. VMAT employs a constantly rotating gantry to deliver IMRT (Greer, 2013). Figure 1.1 shows a schematic arrangement of the components of the head of the treatment machine including the multi-leaf collimator.

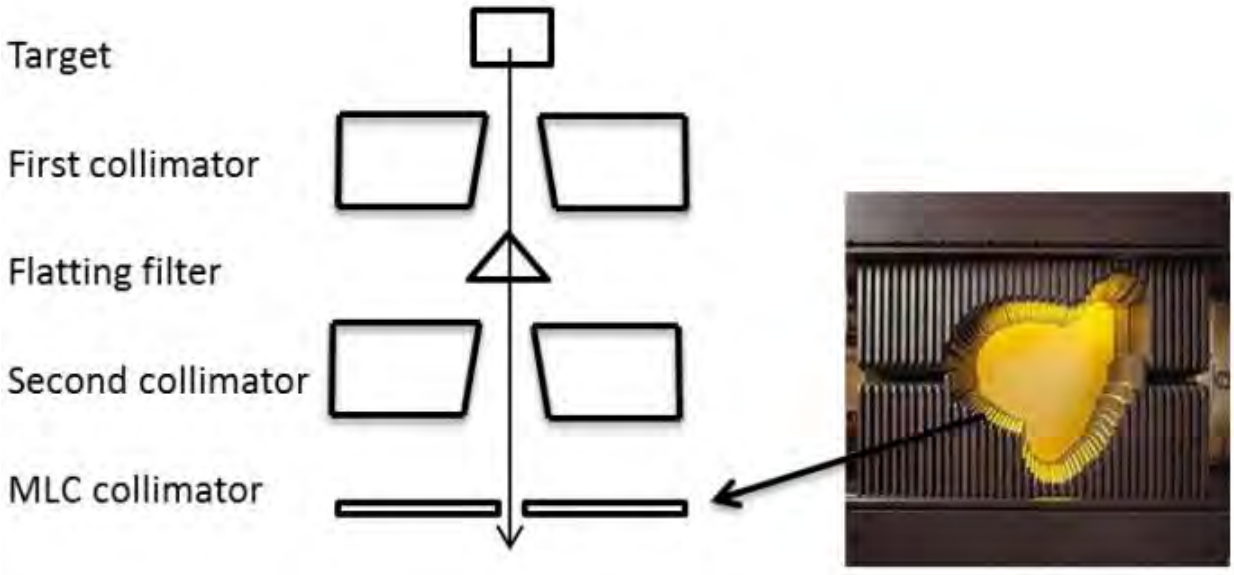

Figure 1. 1: schematic diagram of the gantry components in a Linac and MLC

The treatment which is normally in fractions is planned as to deliver much dose to the target volume while doses as low as possible to the normal tissue. This demands for high dose gradients which makes the plan very delicate to slight variations such as changes in patient anatomical structures as treatments go on. The plan therefore must be reviewed accordingly to adapt to the current anatomical arrangement - Adaptive Radiotherapy (ART). This is laborious and hence not easily adopted.

Due to the irreversible effects of radiation damage, several measures are put in place to mitigate unforeseen errors and uncertainties. The entire procedure is inherent with several sources of error at various levels which eventually affect the optimal performance of the final delivery. Figure 1.2 illustrates the stages of the radiotherapy process in the management of cancer cases, identifying the processes with high error probability.

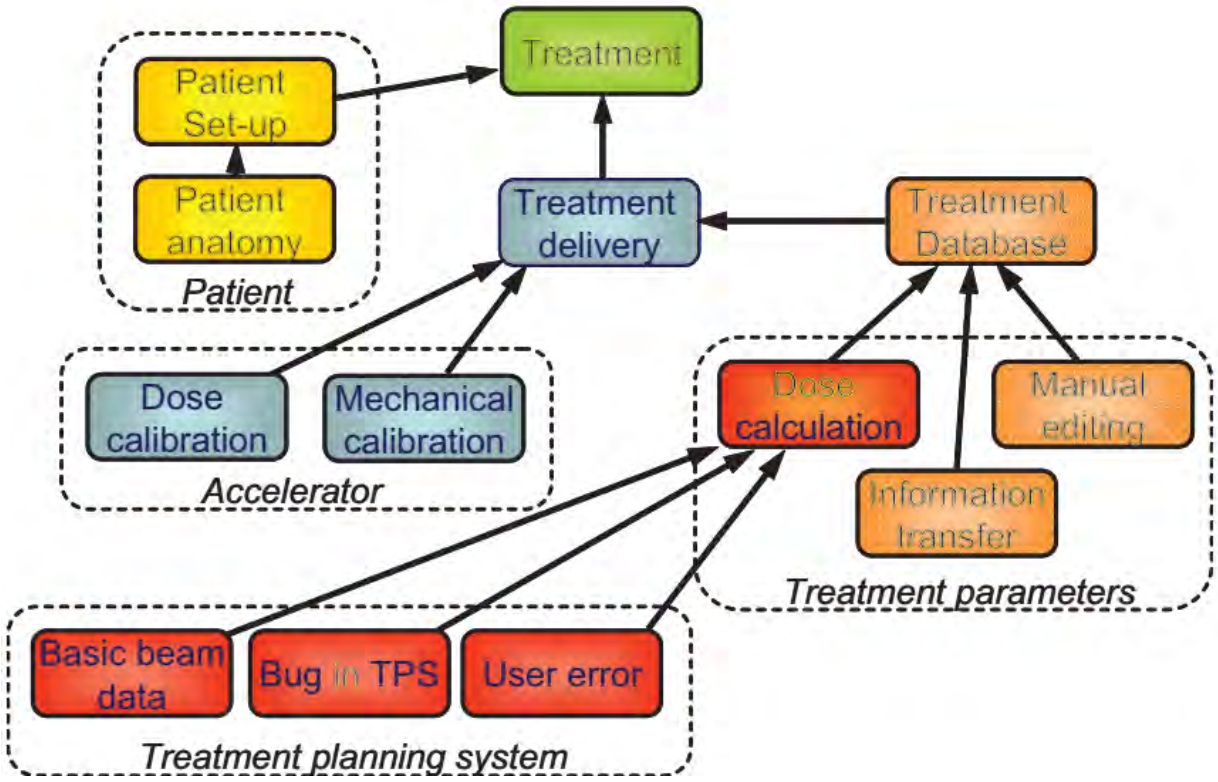

Figure 1. 2: Stages in radiotherapy portraying the high probability of error

Image based dosimetry is a good measure to arrest most of these errors and uncertainties

Due to the increase in the complexity of radiation therapy and their treatment plans, the need for more reliably accurate systems of verification is in high demand. These verification sysems should confidently assist in the determination of the absolute patient's dose distribution at the point and time of treatment. This is done ideally by the electronic portal imaging device (EPID) even though computed radiography (CR) could be a likely replacement in centres where there is no EPID.(Ermott et al., 2007)

Computed radiography (CR) has gained popularity as a good substitute for the conventional screen/film radiography in diagnostic and treatment imaging procedures due to its linear-dose response over several logs of dose. A main setback is its overly energy sensitivity owing to the high Z of the barium in the photostimulable phosphor

(BaSrFBr:Eu^{+2}). The electronic portal imaging (EPI) is the major competitor of the CR in the event of treatment imaging. (Olch, 2005)

Computed radiography (CR) employs the use of a reusable imaging plate (photostimulable phosphor screen) placed in a light-tight casing. The digital patient image is obtained from a readout system after exposure. This system extracts the exposed plate, reads and converts the image into digital form while limiting the exposure of the plate to normal light. The system automatically erases the plate and inserts it back in the cassette afterwards to be reused.(Dance et al, 2014)

1.2 Problem Statement

The Co-60 teletherapy is the major type of treatment procedure for cancer care in Africa and other developing countries. This machine however lacks an online patient dose verification sytem which is required to arrest the errors and uncertainties at the various stages of the process.

This study is therefore targeted at creating an online verification system to monitor patient dose in real time during a Co-60 treatment delivery which will play the same role as the EPID system in the linac. This is done by comparing exit dose distribution readings of the barracuda and a diode with those of a farmer type ionization chamber.

1.3 Research Objectives

The main objective of the study is to develop an online system for patient dose verification in Co-60 teletherapy.

The specific objectives of this study are to;

1 Determine the transmission factor of the treatment couch
2 Measure exit doses using water equivalent and anthropomorphic phantoms
3 Compare dosimetry data from solid state detectors to those of Farmer type ionization chamber

1.4 Relevance and Justification

Precision and accuracy are very important in the discharge of services in radiation therapy in order not to under dose the target volume or exceed the tolerance limits of the organs at risk. This is what makes the quality assurance (QA) procedures as well as the pre and post verification checks a necessity. The need has even come for a verification check during treatment to ascertain the actual dose delivered to the patient since patient protection is of major importance to successful radiotherapy treatment delivery.

This work seeks to create advancement in the QA and QC measures leading to an optimal performance of the treatment by verifying the patient dose using various dosimeters available

1.5 Scope and Delimitation

The research was undertaken at the oncology Directorate of the Komfo Anokye Teaching Hospital, Kumasi, Ghana and was limited to the treatment of prostate carcinoma with external beam. The research protocol and procedures comprised the use

of calibrated ionization chamber, diode and barracuda to measure the patient exit doses and compare with the calculated doses.

1.6 Organization of Thesis

This research is presented in five chapters. Chapter One focuses on the introduction to the study and Chapter Two reviews existing literature relating to the research problem.

Chapter three focuses on the materials and methodology of the study. Chapter four contains the results and discussions whiles Chapter Five presents the conclusions and recommendations from the study. All the relevant works cited in the entire thesis are contained in the reference section.

CHAPTER TWO

2.0 REVIEW OF EXISTING LITERATURE

2.1 General Overview

This chapter reviews the verification needs of radiotherapy with specific interest in in-vivo dose measurements with the cobalt-60 machine and their effects on the final treatment procedure

2.2 Background

The use of ionizing radiation for therapy followed almost immediately after the discovery of X-rays. Innovations involving artificial radioactivity, higher energy X-rays and particle accelerators led to the various types such as photons (X-rays and gamma radiations), protons, electrons and neutrons for therapy. These are delivered by either cobalt 60 unit teletherapy machine or medical linear accelerator as far as external beam therapy is concerned.

2.2.1 Treatment machines

2.2.1.1 The Co-60 machine

The Co-60 teletherapy machines have been in use for the purpose of treatment for several years even though linear accelerators had been in use much earlier even though in limited numbers. The cobalt-60 isotope with a half-life of 5.3 years is produced in a nuclear reactor through neutron activation of the cobalt -57 nucleus according to the nuclear reaction below;

$$^{57}_{27}Co + ^{1}_{0}n = ^{60}_{27}Co + \gamma$$

The Co-60 further decays by beta minus into an exited state Ni-60 which de-exites to ground state with the emission of two gammas of energies 1.17 and 1.33MeV resulting in an average energy of 1.25MeV (Figure 2.1) (Kaur Dhanesar, 2013).

$$^{60}_{27}Co + {}^{0}_{-1}\beta = {}^{60}_{28}Ni$$

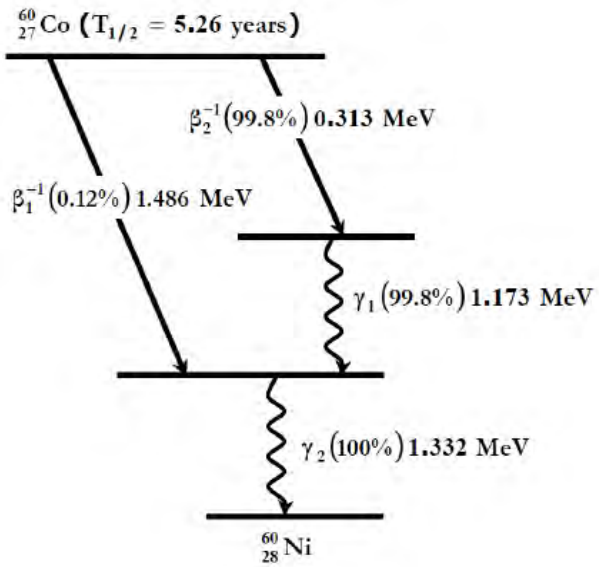

Figure 2. 1: schematic diagram showing the decay of cobalt-60

The cobalt-60 machine as captured in Figure 2.2 below comprises a 360° movable gantry housing the collimators (enabling a wide range of conformal field sizes) and the radiation source, a treatment couch, lasers and a remotely controlled system for calling and retracting the source. It proved very useful and it is the best for a developing country in treatment of cancer patients due to its low cost, low cost of maintenance, minimal power needs and longer source life. Its average energy of 1.25 MeV is relatively lower leading to less penetration making treatment of deep seated tumors very difficult as compared to the linac which comes with a variable dose rates, a set of energies of photon and electron beams and lesser penumbra.

Figure 2. 2: Pictorial view of the CIRUS cobalt-60 machine at the oncology section in KATH

2.2.1.2 Medical linear accelerator

Medical linacs are the mainstay of radiation therapy today. Linacs use microwave radiofrequency RF fields to accelerate electrons to kinetic energies from 4 to 25 MeV in special evacuated structures called accelerating waveguides. The RF fields are produced by magnetrons or klystrons with typical frequency of 2.856 GHz. Since the introduction of first medical linacs, there have been tremendous technological developments that have led to highly sophisticated linacs in comparison with those used in the 1960s. A typical state-of-the-art medical linac is equipped with features such as: dual or triple X-ray energies (from 4 MV to 25 MV), multiple electron energies (e.g. 6, 9, 12, 16, 20 and 25 MeV), independent collimator jaws, dynamic wedge, dynamic multileaf collimator, electronic portal imaging device and computer controlled operation etc as in the Figure 2.3 below (Podgorsak 2005).

Figure 2. 3: A typical medical linear accelerator with its accessories

2.3 Distribution of a Megavoltage Photon Beam Energy within a Patient or Phantom

Interaction of photon with a patient or phantom is characterized by the inverse square law, photon attenuation and scatter. The beam energy deposition along the central axis of a megavoltage beam is as in figure 2.4. The surface dose D_s, is that delivered at the patient's surface with the delivery increasing sharply immediately from beneath the skin to a maximum D_{max} at a depth Z_{max}.

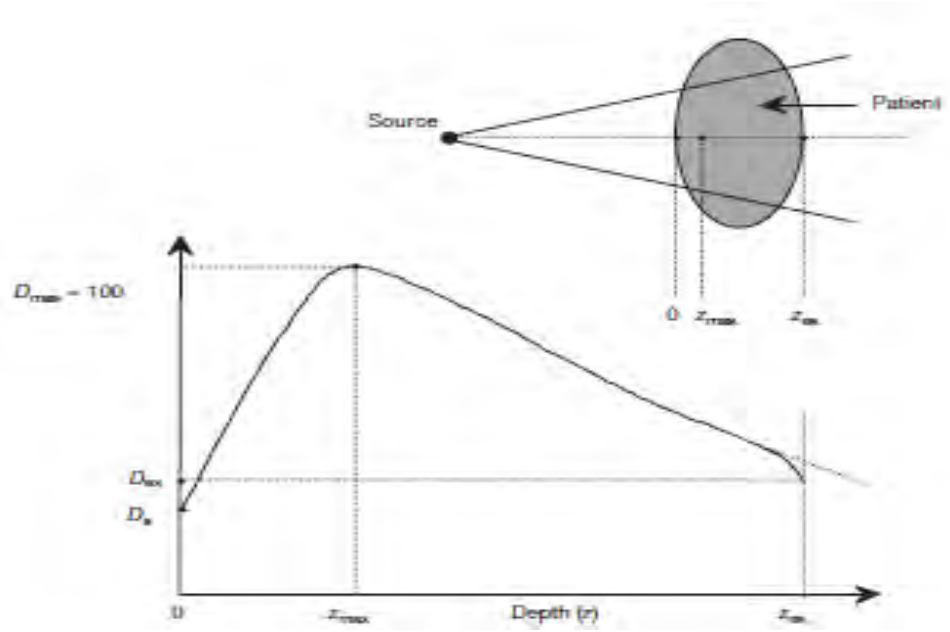

Figure 2. 4: Distribution of photon energy in tissue

2.3.1 Surface dose

Megavoltage beams such as Co-60 have the advantage of the skin sparing effect where the surface dose is much lower than the maximum dose contrary to orthovoltage and superficial beams. Surface dose is proportional to the energy of the beam as well as the field size and is measured using a thin window parallel-plate ionization chamber

2.3.2 Buildup region

Buildup region is the region from the patient surface ,Z= 0 to Z_{max} in the beam and is due the long range of the energetic secondary charge particles released at the patient's surface by photoelectric effect, Compton scatter and pair production which finally deposit their energy within the patient.

2.3.3 Depth of maximum dose (Zmax)

Zmax is the depth into the patient where the greatest dose is delivered. It depends largely on the beam energy and to a small extent on the field size. It is at the surface for orthovoltage and superficial beams, 0.5 cm for Co-60, 5 cm for 25 MV photons. It is generally largest for 5×5 cm^2, decreases for larger and smaller field sizes due to collimator coupled with filter scatter effects and phantom scatter effects respectively.

2.3.4 Exit dose

Exit dose is the dose delivered by the beam as it exits the patient. The deviation from the extrapolated line is due to the energy scatter in air. This can be measured with a parallel plate chamber with its body orientation towards the source (IAEA, 2005).

2.4 Dose Delivery Techniques in External Beam Radiotherapy (EBRT)

2.4.1 Three dimensional conformal radiotherapy (3DCRT)

3DCRT uses a number of radiation beams to deliver the intended dose to the tumor through different angles taking into account the normal tissue toxicity. It takes the advantage of the multi leaf collimator (MLC) system to shape each beam to conform to the shape of the tumor. This technique can be delivered by linac machines but the Co-60 can execute the same technique by employing the use of customized blocks in place of the MLC.

2.4.2 3D Intensity Modulated Radiation Therapy (3D-IMRT)

In 3D-IMRT technique the radiographer moulds and varies the strength of each beam to match the size, shape and position of the tumor and can do this more precisely than conventional or conformal radiotherapy. It deliver much higher doses of radiation to the more aggressive portions of the tumor and smaller doses to the less aggressive parts. The gantry is programed to treat at several beam angles and only irradiates at those positions and cuts before moving to the next position. This allows for the treatment to be just as effective while reducing the side effects (Rührnschopf, E.-P. and Klingenbeck, 2011).

2.4.3 Radiosurgery

Radiosurgery is so named because just like a normal surgical procedure it could be administered in a single day. This is used to treat brain metastasis by delivering large doses of radiation to cancerous brain cells. In order not to cause irreparable damage in the brain tissue those patients always have their heads fixed in customized boxes or masks to minimize movements (Muren, L. P. and Thwaites, 2013). This procedure could be delivered by a linac, cyberknife, VMAT, RapidArc or gamma knife

2.4.4 Proton therapy

This procedure does not make use of the conventional photons but takes advantage of the nature of charged particle interaction of protons to deliver a greater percentage of energy within the tumor. Charged particles are skin sparing and deposit a larger portion of their energy at points underneath the skin (brag peak) which are calculated to coincide with the center of the tumor (Mutic, S. and Dempsey, 2014). In this procedure

normal tissue is spared since all doses fall within the target. Although it is still under trial and experimentation is a better option in the treatment of cancers lying closer to very sensitive tissues such as brain and spinal cord and in most pediatrics cases

2.4.5 Image Guided Radiation Therapy (IGRT)

This involves collecting images to check the tumor position before treatment is given. With this the risk of part of the tumor being missed is reduced. Tumor movement is very common and may be due to changes in patient anatomy as the day to day treatment proceeds, whether the bowl or bladder is filled or empty as well as movements due to breathing. In IGRT images can be acquired by the medical linear accelerator as the patient is in the treatment position and the amount of deviation ascertained to help modify the beams to exactly target the new position of the tumor. Imaging modalities for this procedure could be CT, MRI or PET/CT (Jaffray, 2005).

2.4.6 Volumetric modulated arc therapy (VMAT)

VMAT is a new type of intensity modulated radiotherapy. It works by the medical linear accelerator delivering a continuous beam of radiation while the machine is moving in an arc fashion, changing the beam shape and treatment dose automatically as it moves. It gives the same result as IMRT but several times faster (8 to 9 times) and is sometimes referred to as RapidAarc therapy (Jin, X., Hu, W., Shang, H., Han, C., Yi, J., Zhou, Y., and Xie, 2013).

2.4.7 Stereotactic ablative radiotherapy (SABR)

SABR technique also called stereotactic body radiotherapy, delivers a focused and very high dose radiation onto a tumor in fewer sessions instead of the normal fractionated doses over several weeks offering some patients longer disease and symptom control. It is also sometimes used where surgery is not an option.

2.4.8 Adaptive Radiotherapy

In adaptive radiotherapy procedure, several images and scans are acquired as the treatment goes on and previous treatment plan is revised based on changes of the target volume (shape, size and position). This technique increases the possibility of hitting the tumor and avoiding adjacent normal tissue since some changes may occur during the course of treatment.

2.4.9 Total Body Irradiation (TBI)

Total body irradiation is administered to cancer patients undergoing stem cell transplant. It delivers a heavy dose of radiation or six to eight smaller bits to the entire body with the intention of destroying remnant cancerous bone marrow cells. This depresses the immune system and reduces the likelihood of rejection of the transplant (Harari, P. M., Song, S., and Tomé, 2010).

Even though the whole body is irradiated critical organs such as lung and other vital areas are shielded from the exposure and is normally delivered over three days with two sessions per day.

2.5 Verification Demands of Radiotherapy

Due to the irreversible harmful effects of radiation on the healthy tissues the international institutions emphasized the need for regular in vivo verification to be undertaken and is made mandatory in some countries. This is a very important step towards the delivery of quality health care since the verification can help arrest errors and doubts emanating from position, machine functioning and output, changes in patient anatomy with treatment, organ motion, accuracy in dose algorithm in the TPS and structural outline of patient. Pretreatment delivery of the patient radiation fields to a dosimeter is performed in order to validate transfer of the treatment planning information from the treatment planning system (TPS) to the linac, as well as the deliverability of the treatment (Ezzell et al, 2009). This is not enough verification since the conditions change with the real patient in place and hence the call for verification during the actual treatment.

An error in radiotherapy is simply an unintended deviation in a radiotherapy procedure from what is regarded correct by local protocol. In an attempt to improve safety and quality of radiotherapy, all units are urged to publish radiotherapy errors. The aim was to enable radiotherapy centers to take lessons from those errors in order to prevent future incidence. Examples of those publications are the UK 'patient safety in radiotherapy steering group' reports 2010, 2012 and 2014 (Tan, 2016). A promising field for the detection of errors in radiotherapy is in vivo dosimetry which has exit dosimetry as a component.

In vivo dosimetry could be put into three major divisions: Entrance dosimetry, exit dosimetry, and intracavitary dosimetry (IAEA, 2013). Entrance dosimetry checks the performance and the output of the treatment apparatus as well as the patient set-up

accuracy. In exit dosimetry, apart from checking the dose calculation algorithm, it defines the effect of size, shape, and density variations of patient anatomy on the dose calculation procedure. A diversity of detectors, comprising thermoluminescent dosimeters (TLD), diodes, and detectors like metal oxide silicon field effect transistors (MOSFETs) are presently presented for *in vivo* dosimetry (American Association of Physicists in Medicine, 2005). Choice of a detector could depend on several factors like availability, intrinsic characteristics of detector, measurement type, expertise, cost, and personal preference (Aukett, 1991).

2.5.1 In vivo dosimetric techniques

The development of procedures for in vivo dosimetry towards effective and accurate dose delivery in radiotherapy is a constantly evolving field. It is therefore a necessity to understand the established techniques as well as their strengths and short falls to enable one to improve on them.

2.5.1.1 Entrance and exit dose measurement

It is practically not possible to put a detector inside the patient even though 'in vivo' literally means within the body. It can however be performed within natural openings in the body such as the vagina, rectum and mouth. The immediate possible mechanism is measuring the dose at the beam exit point of the patient (exit dose). This quantity easy to measure and so if done routinely is helpful in detecting some of the uncertainties even though it is limited to those related to machine output variations, patient SSD, inhomogeneities and changes in the thickness of patient. Also, entrance dose measurements are usually carried out with point detectors leave pathways for

dosimetric errors to go unnoticed since such detectors only measure the fluence at a single point instead of the entire field (Curtin-Savard, A. J. & Podgorsak, 1999).

2.5.1.2 Entrance and exit dose midplane dosimetry

A combination of entrance and exit dosimetric measurements is useful in the determination of the dose to the midline of a patient. With these measurements variations in machine output, dose calculation algorithm inaccuracies, setup as well as human error could be immediately detected. The main short fall of this procedure is the simplicity of the calculation algorithms which are based upon a couple of assumptions only valid under ideal (phantom) conditions (Adeyemi A, 1997).

2.5.1.3 Two dimensional (2D) mid-plane dose measurement

Algorithms for one dimensional mid-plane measurements have been improved to two dimensions by measuring the dose at the beam exit point by placing a film at a distance behind the patient. This information is then used in the determination of the dose distribution at the mid plane of the patient in two dimensions. The inaccuracies with this technique were primarily due to large air gaps between detector and patient as well as beam exit surface patient curvatures.

2.5.1.4 The Electronic Portal Imaging Device (EPID)

EPIDs were designed with the same goal as the film for patient positioning except for the online imaging and its digital format. Further experimentation led to the discovery

of its potential use in 2D in vivo dosimetry. Its major setback is failure in predicting accurately the dose at the exit surface for asymmetrical situations.

2.5.1.5 Transmitted dose prediction

This technique compares the measured exit dose during a radiotherapy procedure to a corresponding predicted transmitted dose based on the planned treatment. Any significant difference between these values gives a signal of an error. The procedure requires an accurately calibrated 2D detector as well as an accurate algorithm for the dose calculation and modelling of the transmitted dose. Another drawback of 2D transmission dosimetry is its inability to detect 3D dose errors within the phantom.

2.5.1.6 Monte Carlo based transmitted dose prediction

The prediction of transmitted dose measured by the electronic portal imaging device has been elaborately examined using Monte Carlo models of particles from the gantry all the way to the finest structure of the EPID. Other models such as dosimetric response and calibration of the EPID have also been investigated.

2.6 Dosimeters in External Beam Therapy Quality Assurance (QA)

Several forms of dosimeters are employed in the measurements for patient treatment verification and these include ionization chambers (IC), optically stimulated luminescence detector (OSLD), metal oxide semiconductor field effect transistor (MOSFET), diodes, thermo luminescence detector, radiochromic films, radiographic films, and electronic portal imaging devices (EPIDs)(Tan, 2016).

2.6.1 Ionization chambers (IC)

An ionization chamber is a sensitive air-filled enclosure with three electrodes namely guard, collecting and polarizing electrodes. Radiation interacts with the enclosed air by creating ions within the cavity which are carried by the collecting electrode kept at a high bias voltage and are quantified by an electrometer. The charges are converted into absorbed dose using a calibration factor determined at a primary standard dosimetric laboratory (PSDL).

It measures absolute dose output and is highly recommended due its high level of accuracy and low overall uncertainty of 1.5 percent for absorbed dose to water at reference conditions(IAEA, 2000). Although it affected by ambient weather conditions as well as recombination and polarity effects, the respective factors for their corrections are readily accessible (Khan, 2010).

It however has a few short falls such stem effect, volume averaging as well as the need for bias voltage for its operation.

2.6.2 Diodes

Diodes are crystals of silicon doped with pentavalent and trivalent impurities to create an n-type and a p-type silicon respectively. A typical radiotherapy diode detector is a p-n junction created by mixing a thin layer of n-type silicon with a larger p-type material to create a junction known as the depletion layer which is the sensitive area of the detector. Radiation produces electron-hole pairs in this zone and their migration to the respective terminals generates a measurable current which is to the radiation incident on the detector.

This detector is more sensitive than the ion chamber and this is because the energy needed to create an ion pair in air is about ten folds greater than that needed to create an electron-hole pair. Also the density of silicon is much greater than that of air (1800 times) resulting in the same vast difference in their relative efficiency per volume and hence diode detectors can come in very small sizes. They also have a good spatial resolution, high reproducibility, reliability and have very good linearity in dose response aside their real time dose read out which makes them suitable for in vivo dosimetry (Jormet et al, 1996).

They however portray an energy, temperature, angular and dose per pulse dependence (Mijnheer et al., 2013). The energy dependence traceable to the low Z (Z=14) of the silicon crystal which makes the detector over respond to low energy radiation(Edwards., 1997).

2.6.3 Metal oxide semiconductor field effect transistor (MOSFET)

MOSFET is a semiconductor device comprising a silicon base material with three terminal namely the drain, gate and source terminals. A p-channel MOSFET has an n-type silicon as main base and two p-type regions separated by the p-channel on which lies an insulated silicon oxide (SiO_2) containing the gate terminal.

When no voltage is applied to the gate terminal, no current flows between the source and drain terminals located on the two p-type regions. When irradiated, charges created are permanently trapped causing the threshold voltage ($\mathbf{\Delta V}$) to increase proportionally with the absorbed dose. This detector basically measures the change in threshold voltage ($\mathbf{\Delta V_{TH}}$) from which the absorbed dose is determined.

This type of detector has the advantages such as linearity in dose response, real time readout, water proof, and its small size. A typical micro MOSFET has the dimensions of 1mmX1mmX3.5mm giving it its good spatial resolution and lesser dose perturbation which is desirable for in vivo dose measurements (Jornet et al., 2004).

Just as for diodes, they display over response to low energy radiation owing to the low atomic number of the silicon and the silicon oxide. The device showed values of almost 5 times higher for 33keV than for 6MV photons (Edwards et al., 1997). Some other short falls are its limited lifespan and it not being tissue equivalent.

2.6.4 Thermoluminescent dosimeter (TLD)

A TLD is made by doping a crystalline material to create traps for electrons. They come in the form of rods or chips and contain LiF of atomic number 8.4 closer to that of tissue (Z=7.2).

Exposure to radiation raises electrons from the low energy valence band onto the higher energy conduction band. These electrons later fall back onto the valence band as they dexcite but however caught up within the traps between the two bands where they stay for longer time (metastable state). Heating the crystal releases the trapped electrons and their final dexcitation results in the emission of visible light which is amplified by a photomultiplier tube and converted into electrical current which proportional to the absorbed dose received by the material.

These dosimeters are economical, can be reused, passive dosimeters, have densities similar to tissue, angular independence, have small sizes, and high sensitivity. They

however have a disadvantage of delay reading out process due to time consuming before and after processing.

2.6.5 Optically stimulated luminescent dosimeter (OSLD)

An OSLD consist of a carbon activated aluminium oxide (**Al_2O_3:C**). Its principle of operation is similar to that of the TLD except that light inste4ad of heat is used to stimulate the release of the trapped electrons which must be of a different wavelength from the light emitted by the electrons. Also a light filter is placed on the PMT to selectively absorb preventing the stimulating light from entering (Tan, 2016).

This device is suitable for in vivo dose measurements and has advantages such as high sensitivity, passive dosimeter, small size and no bias voltage needed. It has similar behavior with the TLD regarding angular and temperature dependence; it showed angular dependence of 3 – 4 percent (Kerns et al., 2011) and a variation of 1 percent for a temperature variation of 21^{o}C- 36^{o}C (Yukihara., 2008). The dose response was observed to linear up to 2Gy and super linear thereafter (Reft, 2009) but changes with increasing residual dose of previous exposures (Jursinic, 2010).

Some of its disadvantages include changes in its sensitivity with dose accumulation (>20Gy), its small temperature dependence as well as the inability of the optical stimulation to clear all the effects of the previous radiation leading to increasing background signal.

2.6.6 Radiographic film

This 2D detector consist of a plastic material coated on both or one surface with a radiosensitive emulsion material made up of silver halide (usually AgBr). Exposure of the surface to radiation triggers a reduction reaction which converts the silver ions (Ag^{+}) into metallic silver (Ag) forming a latent image. The remaining unreacted AgBr is removed through the process of fixing. The optical density of the film (degree of blackening) is a measure of the amount of metallic silver deposited on the surface and is proportional to the absorbed dose.

This detector has a very good 2D spatial resolution but its challenges being that the variation of optical density with dose may not be linear and depends on the emulsion. Also the film response is sensitive to varying developer chemical makeup, processing time and temperature. It is also energy dependent owing to the large atomic number of the silver (Z=45) (Van Esch et al, 2004).

2.6.7 Radiochromic film

This is made up of a transparent polyester base with both or a surface covered with a thin layer of micro radiosensitive crystals of a monomer dispersed in a gelatin adhesive. These microcrystals combine with each other when exposed to radiation (Niroomand-Rad et al., 1998) causing the film to gradually change colour to various shades of blue. The blackening of the film is dose delivered by the incident radiation and is measured using a flat-be scanning device in transmission mode (Devic et al., 2005).

The radiochromic film has many merits over the radiographic film such as its insensitivity to light, large dynamic range and does not require chemical processing. Its

main advantage is its low dependence on photon energy which is because it is nearly tissue equivalent(Arjomandy et al., 2010).

2.6.8 Electronic Portal Imaging Device (EPID)

The EPID was crafted with the main intension of patient treatment positioning verification and a replacing the film. It gives a good resolution of a 2D digital visualization and requires no processing unlike film. It is also convenient for pre and real time treatment dose verification since it comes attached to the medical linear accelerator controlled by a robotic arm.

2.6.9 Scanning liquid-filled ionization chamber (SLIC) EPID

This was the earliest EPID developed in The Netherland Cancer Institute, Amsterdam (Meertens, 1985) and eventually gained worldwide use as Portalvision. The matrix of the detector is made of a liquid iso-octane layer which is the active volume, crammed between a pair of printed circuit boards each with 256 strips of electrodes aligned mutually orthogonal to each other between the boards (Van Esch et al, 2004). The intersecting points create a 256 × 256 matrix detector with an active area of 32.5×32.5 square centimeters and a resolution of 0.13×0.13 square centimeters as in the Figure 2.5.

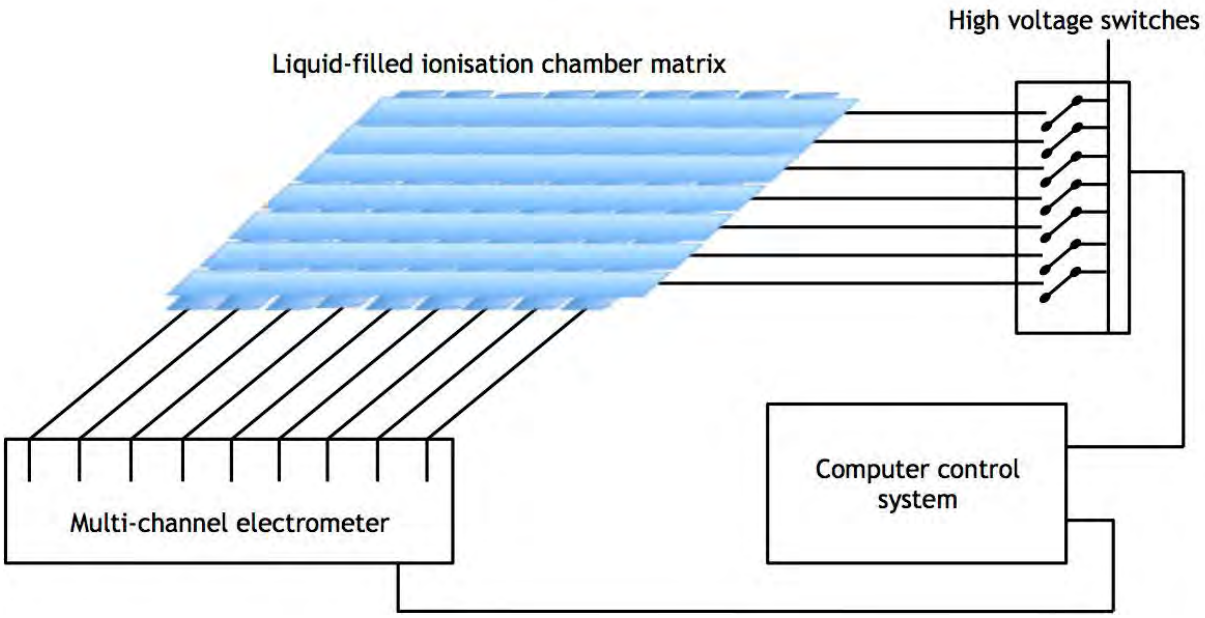

Figure 2. 5: A schematic diagram of the scanning liquid-filled ionization chamber EPID

Creating an image frame begins with a sequential application of a high voltage across the matrix row wise during which time a multi-channel electrometer measures the charge of each ion chamber at the same time as it scans through activated row. The time for frame acquisition is in the range of 1.5 to 6s (Boyer et al., 1992) . The charge measured has been established to be proportional to the square root of the dose rate (Van Herk, 1991) with a little correction factor also proportional to dose rate (Boellaard et al., 1996). With a calibration curve the pixel value of the image can be turned into a 2D matrix of dose rate.

For use as a dosimeter, SLIC EPID has a good short and long term stability with a less than 1% variation (Zhu et al., 1995). It shows a slight energy dependence due to its tissue equivalent response (Curtin-Savard et al., 1999) irrespective of field size and within 0.5% comparable to ion chamber measurements (Zhu et al., 1995). Its main set back its long time of acquisition when or dead time when signal is lost. Averagely, acquiring and storing an image takes 9 seconds (Chang et al., 2000).

2.6.10 Camera based Charge- coupled device (CCD) EPID

The CCD EPID is also an earlier version of an EPID system consisting of a fluorescent screen which a phosphor (Gd_2O_2S:Tb, gadolinium oxysulphide) coated steel plate to convert incident radiation to photons in the visible range. It has mirrors to reflect the visible light which is then imaged by a CCD-based camera. The role of the mirrors is to allow the camera to be placed away from direct exposure which could damage its electronics as shown in Figure 2.6. The commercial CCD EPID (SRI-100, by Phillips Medical Systems, Netherland) has a 40×30 square centimeters fluorescent screen, 512×256 pixel CCD camera andhence a resolution of $0.08\times0.12 cm^2$. other versions of CCD EPID are Beamview Plus (Siemens, USA) and TheraView (Cablon Medical, The Netherlands) (Tan, 2016).

During image acquisition, signals are accumulated on the CCD chip for a predetermined amount of time (0.24 - 1 s) and transferred onto the frame grabber to form a single image frame. Though there is no signal measurement during this time, the dead time is averagely 0.0002s for later versions (Franken et al., 2004). The final image is created by accumulating several image frames within the frame processor. The mode of scanning in this system is not row by row but the entire matrix at the same time and hence faster image acquisition compared to the SLIC EPID. For dosimetric reasons, the number of accumulated frames depends on the time of irradiation which is calculated to cover the entire delivery.

It shows a good stability with a variation of less than 1% for long term and short term response and also showed no dependence on energy though the fluorescent is not tissue equivalent (Pasma et al., 1998).

A common disadvantage of this device is that only 0.01% – 0.1% of the light emited by the phosphor material gets into the camera leading a same percentage of low efficiency

of collection (Herman et al, 2001). Another drawback to its use in dosimetry is the presence of light scattering; where light reflected towards the mirror also falls on and gets scattered by another point on the phosphorescent layer which is finally reflected towards the camera as another signal (Partridge et al, 1999).

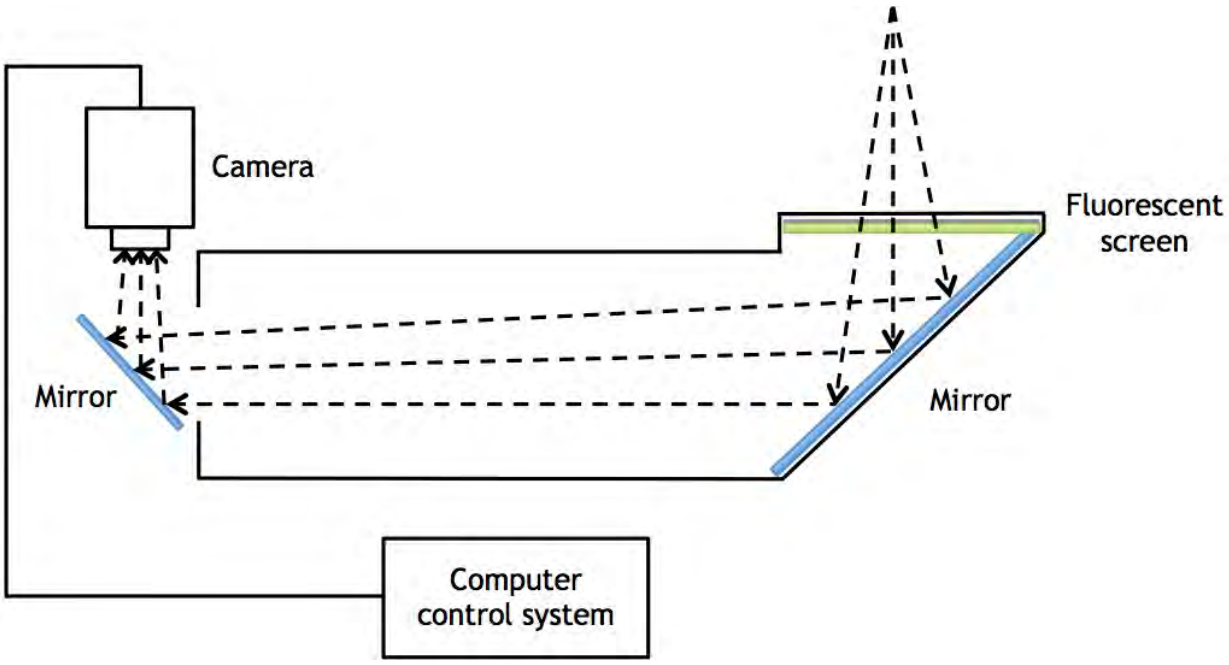

Figure 2. 6: A schematic diagram of the camera based charge-couple device EPID

2.6.11 Amorphous silicon EPID (a-Si EPID)

The a-Si EPID is the most current and widely used model (indirect detection flat panel a-Si EPID) as illustrated in Figure 2.7. It consist of a copper plate which converts incident photons to electrons to increase detection quantum efficiency and also increase image contrast by absorbing scattered radiation which are of low energy. It also has fluorescent material (Gd_2O_2S:Tb) and a system of photodiodes. The fluorescent layer produces visible light from radiation falling on it and has a photodiode array coupled to thin-film transistors mounted on an amorphous silicon panel. The visible light is absorbed by the photodiode and integrates the resulting charge as the thin-film

transistor switches the row wise readout mechanism. The signal read-out, amplification and final digitization are controlled by acquisition electronics.

This system is compact in size, has a better resolution (0.04 cm), fast image acquisition (roughly 0.3 second per frame) generally has a stable response varying by less than 1 - 2% per year (Van Esch et al, 2004) and shows no angular dependence (Kavuma et al, 2008). It displays a quite linear response to dose simplifying the pixel signal conversion to dose. A major problem is its dependence on beam energy due to the chances of photoelectric interaction with the large atomic number phosphor material (Gd_2O_2S with Z=64) which occurs at photon energies below 1 MeV (Kirkby, C. & Sloboda, 2005).

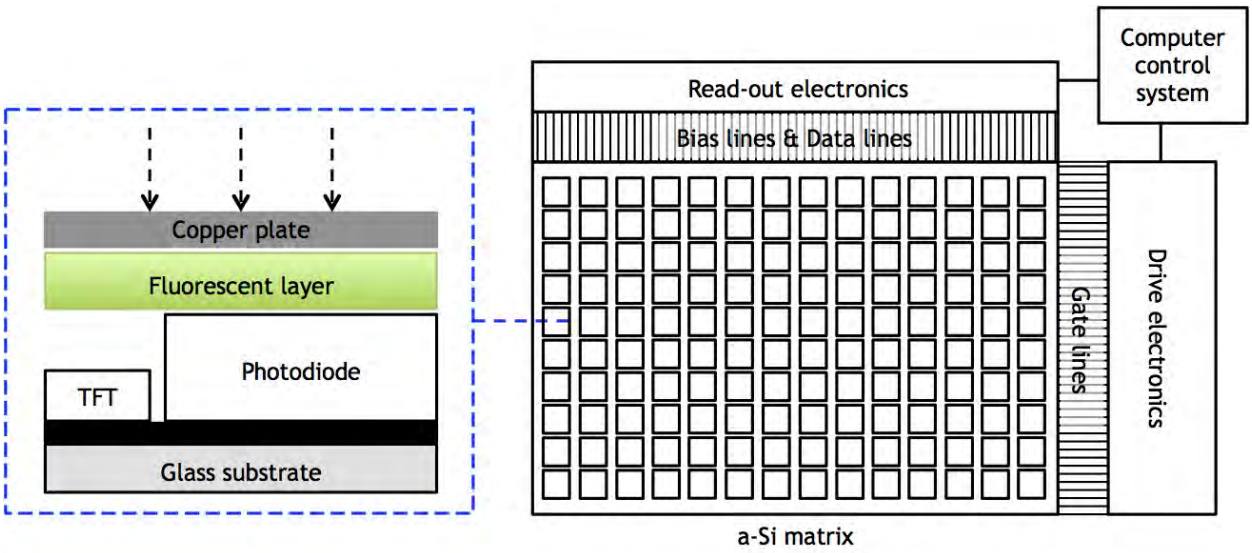

Figure 2. 7: Functional components of the amorphous silicon EPID

CHAPTER THREE

3.0 MATERIALS AND METHODOLOGY

3.1 Materials

The various materials employed in this study included a farmer type ionization chamber, a diode, Barracuda, 30cm×30cm×30cm water phantom, PMMA phantom, an electrometer and a cobalt-60 teletherapy machine

3.1.1 Cirus Cobalt-60 Teletherapy Machine

The Cirus Co-60 teletherapy unit is capable of isocentric treatments and comprises a 130 kg treatment couch, a gantry housing two pairs of symmetric jaws with a smallest field size of 4×4 cm^2 and a maximum field size of 32 cm×32 cm, a collimator system, alignment lasers and a reference source-to-surface distance (SSD) of 80 cm.

The system houses a Co-60 source with a maximum activity of 10785 Ci which is 2 cm in diameter in a lead and natural uranium filled stainless steel drum. The source drawer mechanism is by a pair of dual tunnel air cylinders operating on air under intense pressure. It draws the source between beam on and beam off positions. Figure 3.1 shows the Cirus cobalt-60 teletherapy machine.

Figure 3. 1: the Cirus cobalt -60 teletherapy machine at the Komfo Anokye Teaching Hospital

3.1.2 Farmer-Type Ionization Chamber

The ionization chamber used for this work is the Farmer type by PTW Freiburg with model and serial numbers of W-30010 and 129 respectively (Figure 3.2). Its absorbed-dose-to-water calibration coefficient ($N_{D,W}$) was used together with absorbed-dose-to-water based protocols (i.e. TRS-398) to estimate the absorbed-dose-to-water in clinical settings and the reference check source measurements. The substitution method was used for its calibration using the IAEA reference standard chamber NE-2561/NPL (#321). The calibration coefficients were determined at a temperature of 20.0 ^{0}C, Pressure of 101.325 kPa and a Relative Humidity of 50.0%. Its absorbed-dose-to-water ($N_{D,W}$) was 5.3 nC.

Figure 3. 2: Farmer type ionization chamber (PTW Freiburg, Germany)

3.1.3 Acrylic (PMMA) Phantom (Slabs)

Acrylic phantom material is a clear plastic known as polymethylmethacrylate (PMMA) but is also widely known by names such as Perspex, Lucite, Plexiglas etc. It has an effective density of 1.185 g/cm^3 and can be obtained in several different dimensions. It is used extensively in the medical physics profession for output calibration, energy check, calibration of electron beams and film dosimetry and are readily designed to hold the various detectors. In this study, a 30 cm × 30 cm Perspex material (slabs) with respective thicknesses of 1 cm and 2 cm were used, as shown in Figure 3.3.

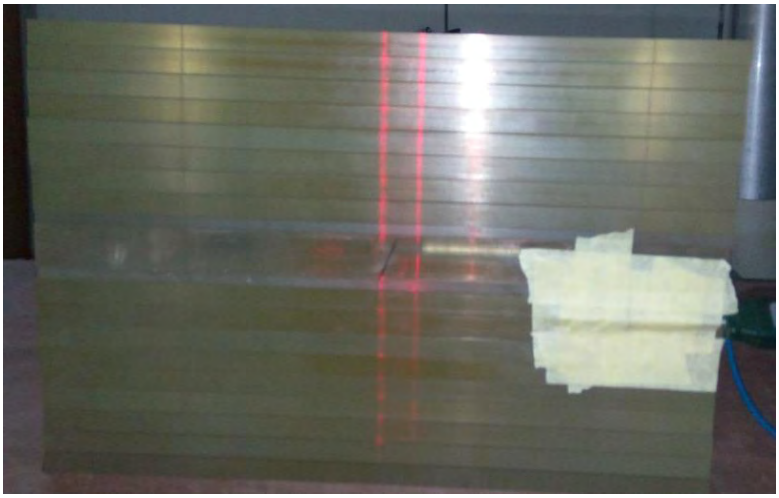

Figure 3. 3: Perspex (PMMA) phantom

3.1.4 Water Phantom

The water phantom used in this study has dimensions of 30×30×30 cm^3 and is made from a 1cm thick clear Perspex material which is easy to see through. It has an aluminium component for holding the detector at the various depths as can be seen in Figure 3.4 below.

Figure 3. 4: A 30×30×30cm3 water phantom

3.1.5 Diode

The diode used in this work is the **IBA PFD^{3G} Photon Dosimetry Diode** produced by Radiation Products Design, Inc. based on the third generation pSi semiconductors. It is a high doped p-type Si diode with an active area diameter of 2 mm, an active volume thickness of 0.06 mm and a sensitivity of $3x10^7$ Gy/C. It is specially designed for both in air and in water depth dose and profile measurements in small photon beams. It is water proof, independent of energy, dose rate, bias, pressure and humidity and is robust, very reliable and needs no "warm up" time. Figure 3.5 shows a pictorial view of the IBA PFD^{3G} Photon Dosimetry Diode.

Figure 3. 5: Pictorial view of IBA PFD-3G Photon Dosimetry Diode.

3.1.6 Barracuda (kilovoltage solid state detector)

The barracuda used in this study is a product of RTI electronics with serial and model numbers as BCI-08110025 and BCI-081125 respectively. The detector system is composed of a cabinet containing at least a module, a multi-purpose detector (MPD) and a handheld computer with the QABrowser software as in Figure 3.6. The QABrowser controls the Barracuda and provides an easy to use user-interface. The

instrument's set-up depends on the mode of measurement; real-time display (RTD) and application mode.

In real-time display mode "virtual" meters display real-time data. Up to six values can be measured and displayed at the same time. The in-built applications allow different tests such as accuracy, reproducibility, linearity, HVL, and CTDI. There are also applications for viewbox test and monitor test using the light detector. The QABrowser also shows waveforms and log data.

Figure 3. 6: The Barracuda system; cabinet, multi-purpose detector and a palm-held computer

3.1.7 Prowess Panther Treatment Planning System (TPS)

This brand has a competitive advantage over several others by offering 3D conformal therapy on the familiar and easy to use Windows platform (Window XP). Users are able to generate treatment plans quickly due to the familiar Windows®. The version used at KATH is v.4.60.

3.1.8: Electrometer (PTW Unidos)

The electrometer used for measurements during this work is the PTW UNIDOS electrometer (serial number T10005-50316, PTW, Freiburg, Germany).

The ionization chamber and diode were connected to the Unidos electrometer as shown in figure 3.7 for all the measurements with those detectors.

Figure 3. 7: PTW Unidos Electrometer

3.1.9 Anthropomorphic phantom

The phantom used for this work is an adult female produced by Atom Dosimetry Verification Phantoms. It is made of 38 sections entirely from a tissue equivalent epoxy resin and weighs 55 kg with a thoracic dimension of 20×25 cm^2. It has a model number of 702 and a physical and electron densities of 1.6 g/cc and 5.03×10^{23}/cc. figure 3.8 shows a photo of the anthropomorphic phantom.

Figure 3. 8: Anthropomorphic phantom

3.2 METHODOLOGY

3.2.1 Couch Transmission Factor

In measuring the treatment couch transmission factor, a water phantom of dimensions 30×30×30 cm^3 was set up isocentrically on the treatment couch using the alignment lasers of the Cirus Cobalt-60 machine. An ionization chamber (Farmer chamber, PTW, Freiburg, Germany) was placed at depth of 10 cm within the phantom as recommended by Olch et al. (Olch et al, 2014) at 80 cm Source to Surface Distance (SSD). Set up for the study is shown in Figure 3.8.

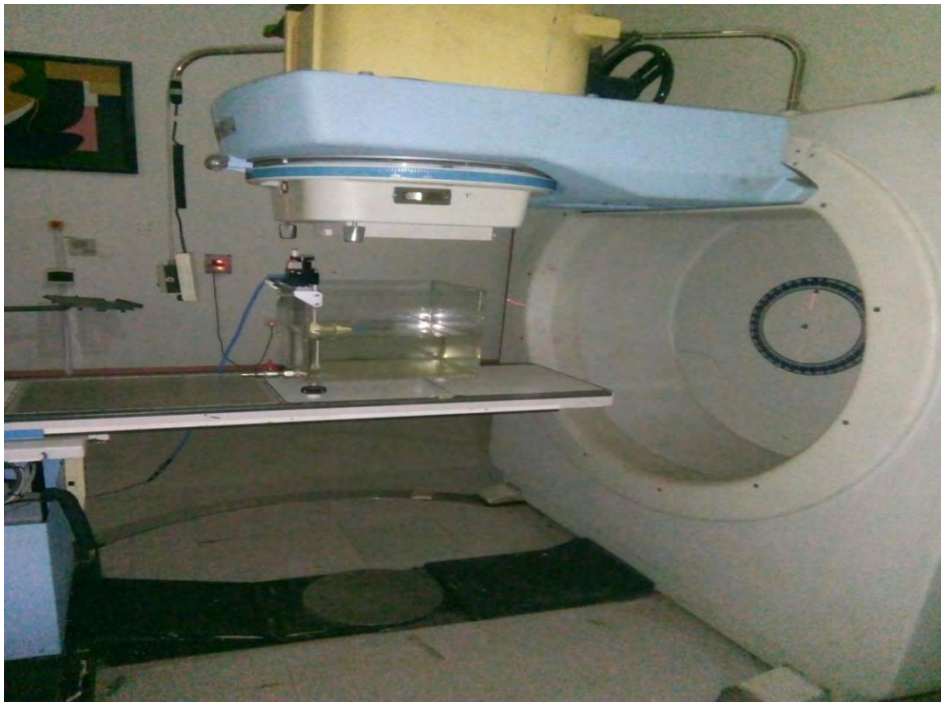

Figure 3. 9: Setup for couch transmission factor determination

A range of field sizes from 4×4cm^2 to 32cm×32cm^2 were used with 10×10 cm^2 as the reference field size and a treatment time of 1min was used for all the readings. Five replicates of ionization chamber readings were recorded for each field size and ionization chamber position (0 cm, 5 cm, 10 cm, 15 cm and 20 cm) for pairs of opposite gantry angles (i.e 360^o and 0^o, 60^o and 240^o, 30^o and 210^o, etc) using the UNIDOS electrometer.

The initial and final temperature and pressure of the treatment room were measured and recorded and used for the temperature and pressure correction using Equation 3.1 since the detector was calibrated at standard conditions (i.e. T_o = 22°C and P_o = 101.325 kPa).

$$K_{cor} = \frac{273.2+T}{273.2+20.0} \times \frac{101.325}{P} \qquad (3.1)$$

Where T is the temperature in degrees Celsius, P is the pressure in kilopascals and K_{cor} is the correction factor.

The average readings were then multiplied by the correction factor, K_{cor} to acquire the corrected reading:

$$M_{cor} = M \times K_{cor} \qquad (3.2)$$

Where M is average ionization chamber reading and M_{cor} is the corrected average ionization chamber reading

The transmission factor of the treatment coach was calculated for each detector depth as the ratio of measured value with treatment couch M_{couch} (eg gantry angle 180°) to that without treatment couch $M_{nocouch}$ (eg. Gantry angle 0°):

$$TF = \frac{M_{couch}}{M_{no\ couch}} \qquad (3.3)$$

3.2.2 Diode Calibration measurements

The diode calibration was done using the 30cm×30cm Perspex slab phantom arranged at thicknesses of 0.5 cm, 1.5 cm, 2.5 cm, 3.5 cm, 10.5 cm, 12.5 cm and 15.5 cm above the detectors. The farmer ionization chamber connected to the Unidos electrometer was irradiated at each depth in turns at field sizes of 5×5 cm^2, 6×6 cm^2, 8×8 cm^2, 10×10 cm^2, 12×12 cm^2, 15×15 cm^2, 20×20 cm^2, 25×25 cm^2, and 30×30 cm^2 with the same treatment time of 1min and 10×10 cm^2 as the reference field size. This was done at a source to surface distance of 80 cm and gantry angle at 0°. Replicates of three electrometer readings were recorded for each field size and an average value calculated. The mean readings were corrected for temperature and pressure effects by using Equation 3.1

The ionization chamber was replaced with the diode in the same setup and procedure repeated except that there was no need for temperature and pressure correction for those readings since the diode is not vented to air.

The calibration factor ($\mathbf{F_{cal}}$) was determined as the ratio of ionization reading at the depth of maximum dose to that of the diode at the same position at a field size of 10×10cm^2 and source to surface distance of 80 cm and gantry angle of 0°

$$\boldsymbol{F_{cal} = \left(\frac{D_{ic}}{R_{diode}}\right) at\ ref.cond} \qquad \textbf{(3.4)}$$

The correction factor for field size ($\boldsymbol{CF_{FS}}$) was determined as the ratio of ion chamber reading to diode reading at any field size $\boldsymbol{a}$ normalized with reference conditions (FS = 10x10cm^2) as given by Equation (3.5). Equation 3.6 was used in the determination of the depth correction factors estimated using the reference field size at the various depths normalized with the factor at the depth of 0.5cm.

$$\boldsymbol{CF_{FS} = \frac{(D_{ic}/R_{diode})}{(D_{ic}/R_{diode})} \frac{(at\ FS = a)}{(at\ FS = 10x10)}} \qquad \textbf{(3.5)}$$

$$\boldsymbol{CF_{D} = \frac{(D_{ic}/R_{diode})}{(D_{ic}/R_{diode})} \frac{(FS = 10x10\ at\ any\ depth)}{(FS = 10x10\ at\ d = 0.5cm)}} \qquad \textbf{(3.6)}$$

3.2.3 Exit Dose Measurements

The setup for the exit dose measurement is as illustrated by Figure 3.10 and Figure 3.11. The Perspex slab phantom was arranged into a thickness of 7cm on the treatment couch at SSD of 80 cm and gantry angle at 0°. The ionization chamber was clamped on a retort stand and positioned at a distance of 30 cm below the treatment couch with its build-up cap on. A treatment time corresponding to a dose of 200 cGy at that depth and the various field sizes (ie. Square fields of sides 5 cm, 7 cm, 10 cm, 12 cm and 15 cm) was

calculated and delivered. Exit signals were measured at the beam axis and at four other points around the center of the beam which was accurately done by placing the retort stand on a calibrated card taped to the floor. These measurements were taken for each of the field sizes and repeated for 10 cm, 12 cm and 15 cm phantom thicknesses. The entire procedure was repeated using the anthropomorphic phantom with the same treatment times corresponding to the various thicknesses and field sizes. The mean readings for field size was determined and corrected for temperature and pressure effect using Equation 3.1.

The same procedure was repeated for the diode and Barracuda in turns and the readings tabulated.

Figure 3. 10: set-up for ionization chamber exit dose measurements under anthropomorphic phantom

Figure 3. 11: Set-up for barracuda exit dose measurements under Perspex slab phantom

3.2.4 Dose Calculation with Prowess Panther Treatment Planning System

All the treatment times used in the irradiation at different thicknesses of Perspex and anthropomorphic phantoms were calculated except for that used for the diode calibration. Computed tomography (CT) images of both phantoms were acquired and uploaded into the Prowess Panther treatment planning system. It was from these images that the various treatment times for depths and field sizes were calculated and used for the irradiation

3.3 Analysis

The Microsoft Excel 2013 which is a component of the 2013 version of Microsoft Office, was used in the entire analysis of the data obtained in the study. This data processing and analysis included the determination of the mean electrometer readings,

temperature and pressure correction factors, couch transmission factors, the diode calibration factors and the deviations between them as well as all the graphs plotted from the study.

CHAPTER FOUR

4.0 RESULTS AND DISCUSSION

4.1 Introduction

This section contains the findings as well as the discussions of the findings of the study. The transmission factor of the couch and its dependence on field size and depth are discussed. The various calibration factors of the diode and their dependent quantities are also discussed. Finally, discussions are also done on the comparison of the exit dose measurements by the various detectors.

4.2 Couch Transmission Factor

The couch transmission factor was estimated to ascertain the impact of the treatment couch on the exit doses measured. This was done by taking measurements with an ionization chamber at various depth in a 30×30×30 cm^3 water phantom and at different field sizes at gantry angles 0^o and 180^o. The measurements for this calculation as well as the transmission factors are presented in appendix A and B. Equation 3.3 was used for the computation and the factor determined from the average of the values from the reference field size (10×10) which was 0.97 at a depth of 15 cm. This implies that 97% of the beam is transmitted while 3% is attenuated by the treatment couch. From Figure 4.1 it can be observed that the factor increases steeply from the minimum field size until field size of 8×8 cm^2 where it becomes almost constant with increasing field size. The factor however decreases with depth of the detector in the phantom.

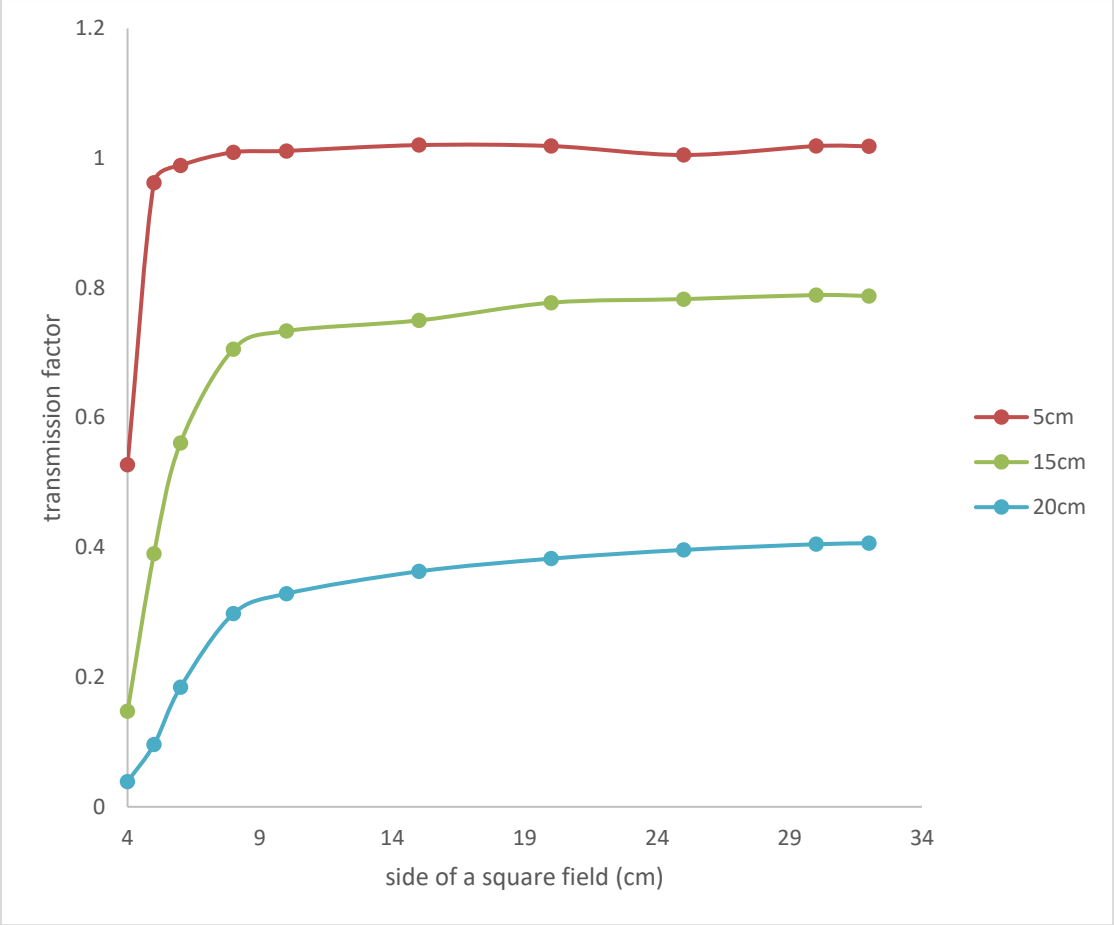

Figure 4. 1: A graph showing the variation of the couch transmission factor with field size and depth

4.3 Detector Calibration

4.3.1 Diode Calibration Factor

The calibration factor ($\mathbf{F_{cal}}$) of the diode was determined with measurements using the PMMA water equivalent slab phantom by irradiating the ionization chamber and diode at the depth of maximum dose in turns with the same treatment time of 1min with a SSD of 80 cm. The factor was calculated by applying Equation 3.4 on measurements at the reference field size and the factor was 0.04404 signal which was used in the study. This value is comparable to the values published of PFD-3G diodes by Jornet et al (Jormet et al, 1996). Even though this value is satisfactory for its use in this study it is recommended that recalibration is done regularly since the sensitivity of diode detectors

vary with accumulated dose (Adeyemi A, 1997).

4.3.2 Field Size Correction Factor

There was the need to correct the readings for field size since different field sizes were used in the study. The setup and procedure was the same as those for the calibration factor determination. The calculation was done using Equation 3.5 at a particular depth and the factors ranged from 0.916284 to 1.028609 with a standard deviation of 0.04275 as in Table 4.1 below. The factor was also noticed to increase slightly at the smaller field sizes and then decrease gently shortly afterwards. It generally decreases with field size due to the increase in absorbed dose resulting from more scatter as field size increases as is shown in Figure 4.2. The two detectors are exposed to the same conditions but the differences lie in the differences in their modes of detection; while an energy of 33 eV is required to create an ion pair in air, only 3 eV is needed to create an electron-hole pair in the crystal of the diode. Also the ion chamber is more sensitive to scatter radiation than the diode.

Table 4. 1:Field size correction factors at the various field sizes at a depth of 15.5cm

Field size	**Field size correction factor CF_{FS}**
5x5	1.028609
6x6	1.031845
8x8	1.017079
10x10	0.999988
12x12	0.989861
15x15	0.97441
20x20	0.947606
25x25	0.929183
30x30	0.916284
	St. dev = 0.04275%

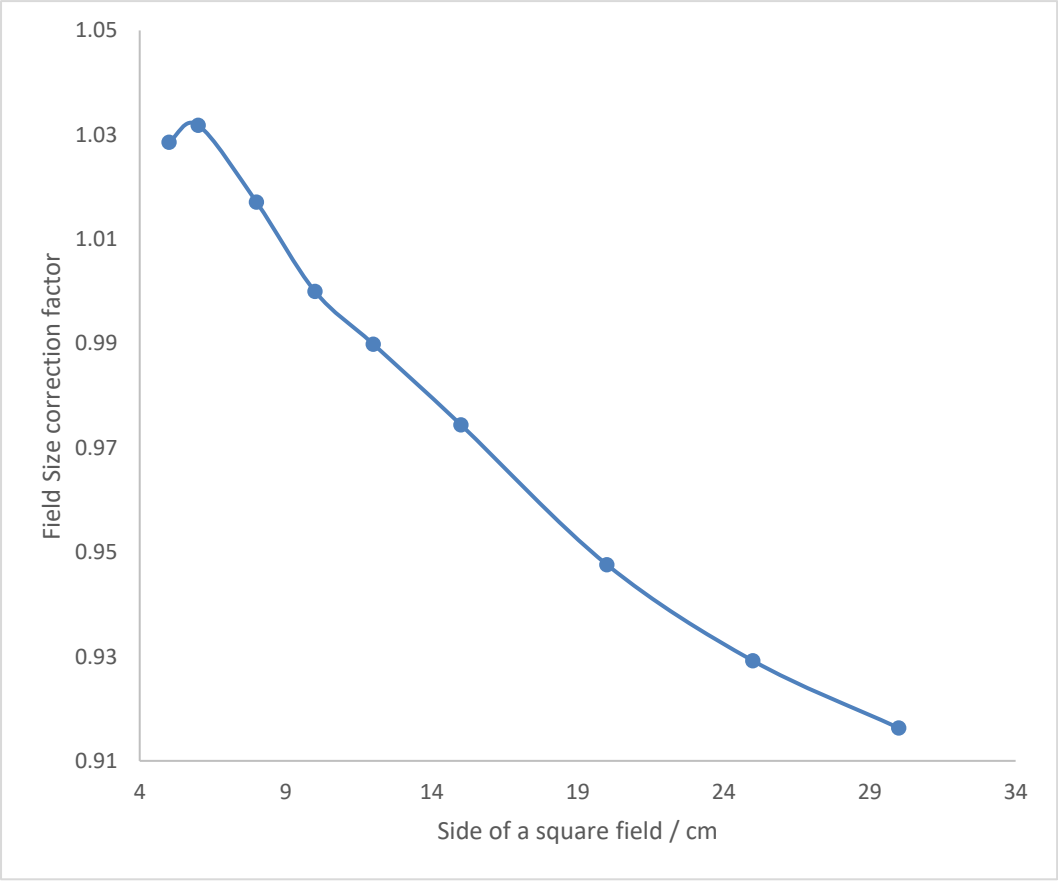

Figure 4. 2: Variation of field size correction factor with field size at depth of 15.5 cm

4.3.3 Phantom Thickness Correction Factor (CFD)

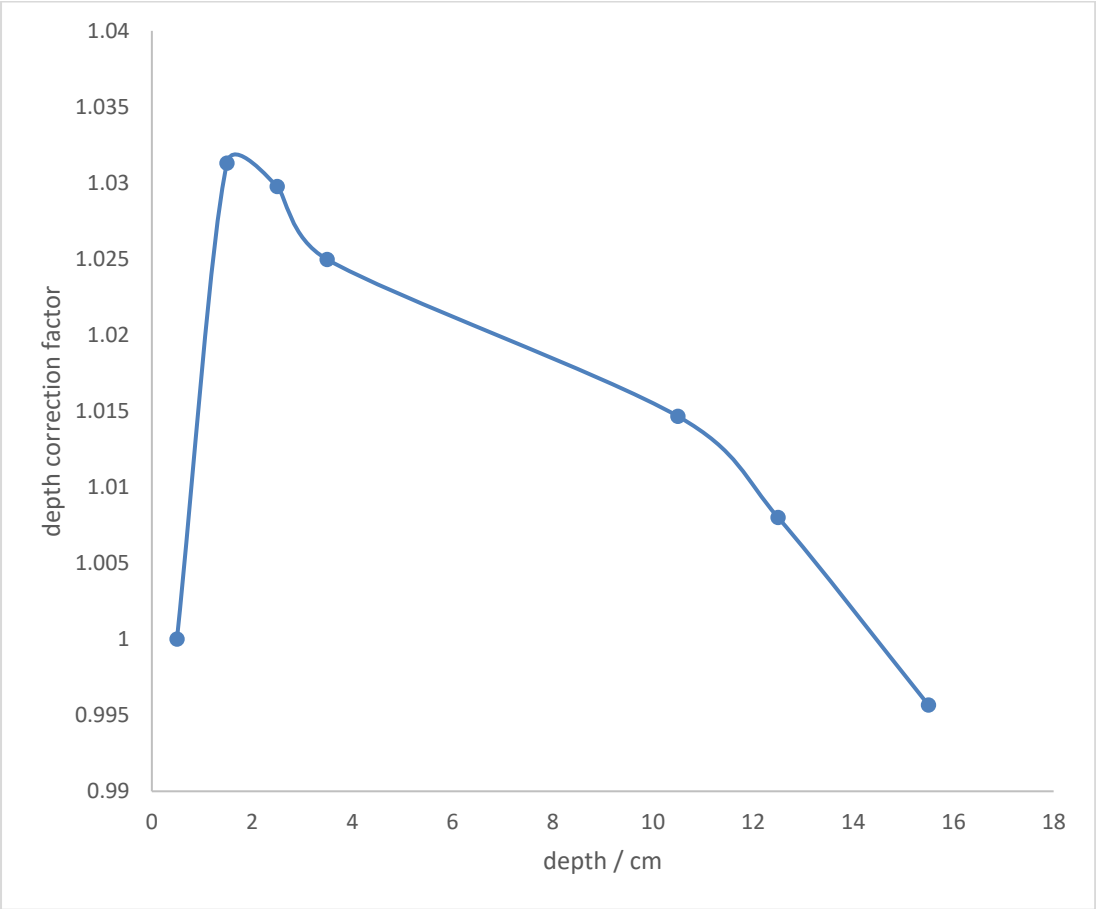

Figure 4. 3: Variation of depth (thickness) correction factor with slab phantom thickness at 10×10 field size

The Figure 4.3 above shows how the thickness correction factor varies with phantom thickness. As the phantom thickness increases, the scatter due to the phantom increases accordingly but the ion chamber is more sensitive to scatter radiation than the diode, the correction factor increases according to Equation 3.6. Further increases in thickness leads to increased beam hardening which decreases dose rate. Once again the ion chamber is more sensitive to dose rate than the diode and therefore increasing thickness led to a decrease in the correction factor.

Table 4. 2: Phantom thicknesses with their corresponding correction factors

Thickness/ cm	Thickness correction factor (CF_D)
0.5	**1.000004**
1.5	**1.031311**
2.5	**1.029757**
3.5	**1.024968**
10.5	**1.014656**
12.5	**1.008**
15.5	**0.995675**
	Sd = 0.0143%

It can be noticed from table 4.2 that the variation of the correction factor is about 0.014% which is different from that reported by Jormet et al which was 0.1% and this can be attributed to the rapid decrease in dose in Cobalt-60 as compared to the 18 MV photon beam which was used by Jormet (Jormet et al, 1996).

There was no need for angular, SSD and energy correction factors since all the measurements were done at gantry angle of 0^o and the SSD and energy was 80 cm and 1.25 MeV respectively.

The calibration factor of the Barracuda, which is a diagnostic detector was also determined for the megavoltage energy range where its readings were compared to those of the ionization chamber. The set of data showed a linear relationship with a high correlation coefficient of 0.9448 even though the Barracuda readings were smaller (in mGy) as illustrated in Figure 4.4 below. The calibration factor which was determined by applying Equation 3.4 at the reference field size and at depth of 10 cm and was found to be 6.343, was used in the correction of the Barracuda readings.

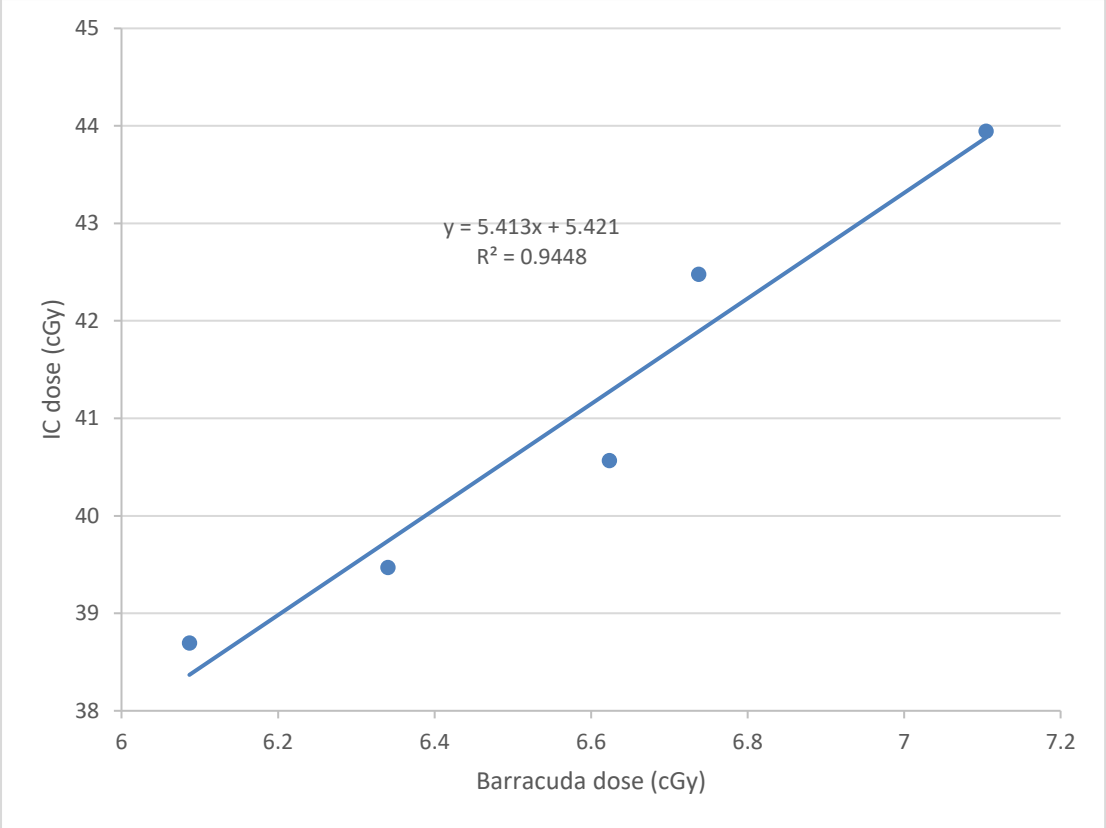

Figure 4. 4: A graph of ion chamber readings against Barracuda readings at depth of 7cm

4.4 Exit Dose Comparison

The exit dose measurements were done using the setups as illustrated by Figure 3.10 and Figure 3.11. Each of the detectors was placed 30 cm underneath the couch along the beam central axis and the phantoms irradiated at various field sizes and depths with a treatment time equivalent to 200 cGy with a SSD of 80 cm.

Comparing the exit doses measured by the ionization chamber to those of the diode and the Barracuda, it is evident that the measurements were very comparable since they show less deviation from each other. This clearly shows that the calibration and correction factors were accurately determined with the right methods. Figure 4.5 and figure 4.6 below show how each of the detector doses compare with those of the ionization chamber.

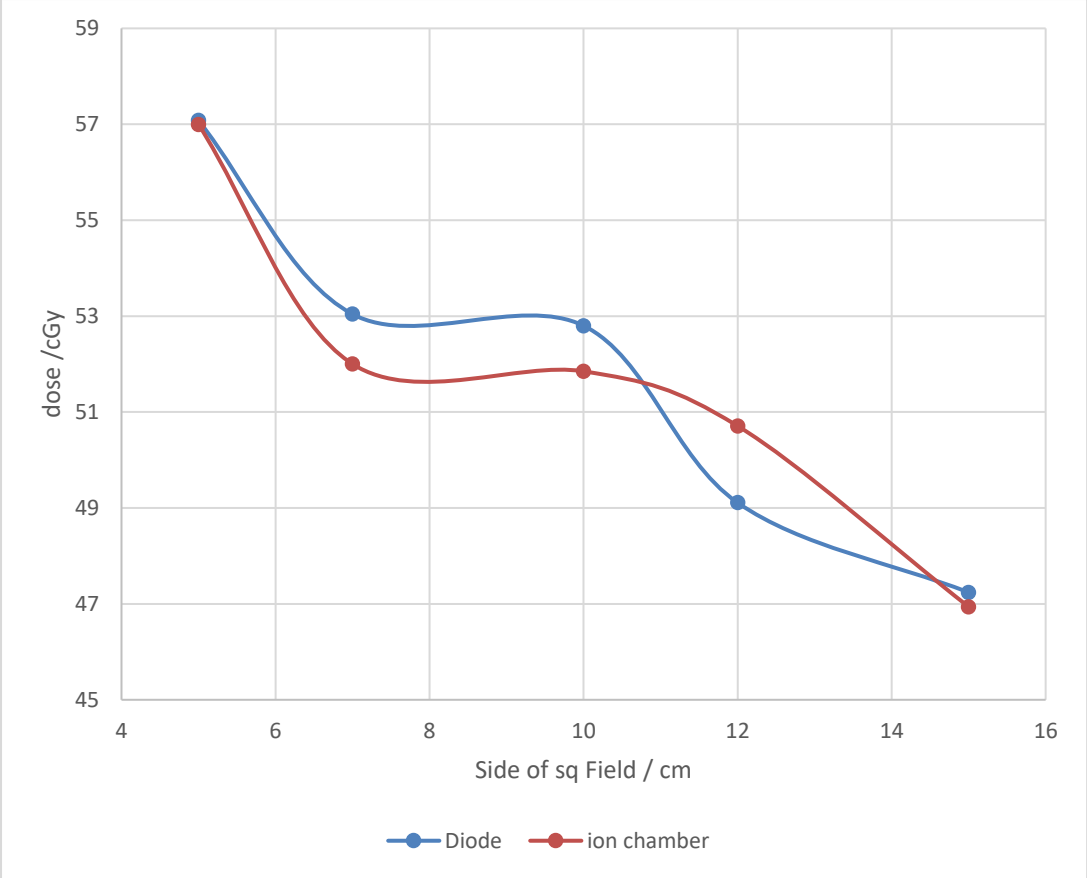

Figure 4. 5: A graph of dose against field size at a depth of 10cm in anthropomorphic phantom

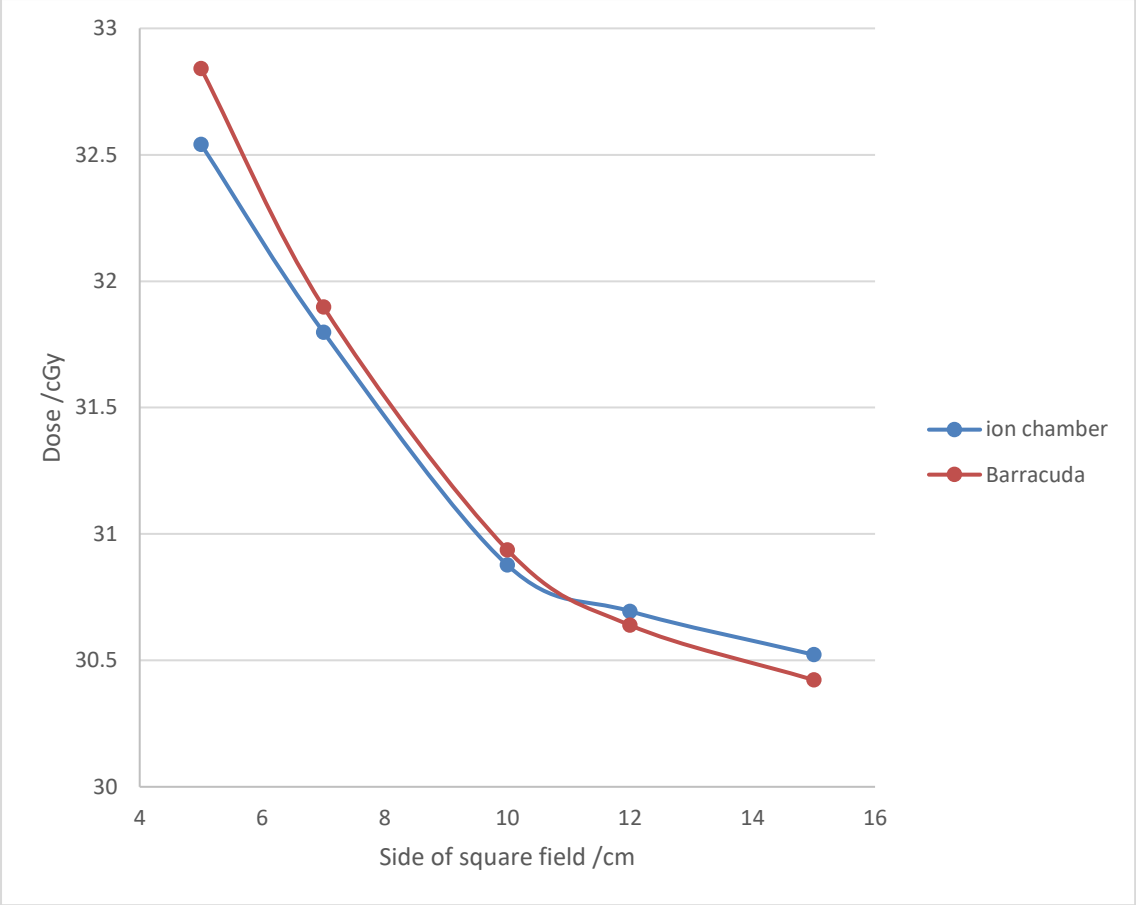

Figure 4. 6: A graph of dose against field size at a depth of 15cm in anthropomorphic phantom

The percentage deviation between the measurements generally was less than 2% for both detectors which confirms the accuracy of the estimated correction factors. It also makes the measurements by the two detectors very reliable since they compared so well with those of the reference detector (ionization chamber). The consistent deviation for a particular field size implies the field size correction was very well estimated. The recorded measurements of the various radiation detectors are presented in the Appendix B.

CHAPTER FIVE

5.0 CONCLUSION AND RECOMMENDATIONS

5.1 Conclusion

In vivo dosimetry by exit dose measurement is a very promising area for better dose verification and general QA in the field of radiotherapy. The practice of in vivo dosimetry is mandatory in only a few countries due to social and economic reasons.

From the findings of this study it is evident that in vivo dosimetry by exit dose measurement is a potential tool to raise the quality of cancer care. The Barracuda corrected readings were comparable to those of the ionization chamber with deviations of less than 2%. This device gives a real time dose measurement and hence can be adopted for in vivo dosimetry since its correction factor can be accurately determined. The readings of the diode which is ideally meant for in vivo dosimetry deviated minimally from the ion chamber readings (less than 2%) for all field sizes under the study and hence can be considered reliable. This notwithstanding, all the necessary correction factors must be carefully determined. These measured exit doses can then be reconstructed with the appropriate computer software to generate the patient doses which can be verified with the TPS generated values as part of quality assurance.

5.2 Recommendations

5.2.1 Regulators and Policy Making Body

It is recommended that appropriate policy are drawn to initiate and implement in vivo dosimetry and ensure the staff involved acquire the needed training.

5.2.2 Clinical Community

It is recommended that the hospital management adopt the diode dosimetry protocol for all treatment regimens as part of Quality Assurance

It is also necessary to set up a QA committee if not available to improve and maintain quality culture in the clinical setting

Also close supervision by a medical physicist is very necessary during in vivo dosimetry.

5.2.3 The Research Community

More work can be done in this area by developing a dose reconstruction algorithm which could reconstruct the patient dose from the exit dose measurements and then compare that with the TPS generated dose.

REFERENCES

(IAEA), I. A. E. A. (2013). Development Procedures for in vivo Dosimetry in Radiotherapy. IAEA Human Health Reports No. 8, (8).

American Association of Physicists in Medicine, A. (2005). Diode in vivo Dosimetry for Patients Receiving External Beam Radiation Therapy. Report of Task Group 62 of the Radiation Therapy Committee 2005: Report 87. New York: American Institute of Physicists.

Arjomandy, B., Tailor, R., Anand, A., Sahoo, N., Gillin, M., Prado, K. &, & Vicic, M. (2010). Energy dependence and dose response of Gafchromic EBT2 film over a wide range of photon, electron, and proton beam energies. *Medical Physics*, *37*(5), 1942–1947.

Aukett, J. (1991). A comparison of semiconductor and thermoluminescent dosemeters for in vivo dosimetry. Br J Radiol 1991;64. *British Journal of Radiology*, (64), :947-52.

Boellaard, R., Van Herk, M. & Mijnheer, B. J. (1996). The dose response relationship of a liquid-filled electronic portal imaging device. *Medical Physics*, *23*(9), 1601–1611.

Boyer, A. L., Antonuk, L., Fenster, A., Van Herk, M., Meertens, H., M., & P., Reinstein, L. E. & Wong, J. (1992). A review of electronic portal imaging devices (EPIDs). *Medical Physics, 19*(1), 1–16.

Chang, J., Mageras, G. S., Chui, C. S., Ling, C. C. & Lutz, W. (2000). Relative profile and dose verification of intensity-modulated radiation therapy. *International Journal of Radiation Oncology Biology Physics*, *47*(1), 231–240.

Curtin-Savard, A. J. & Podgorsak, E. B. (1999). Verification of segmented beam delivery using a commercial electronic portal imaging device. , 26 (5),. *Medical Physics*, *26*(5), 737–742.

Dance, D. R., Christofides, S., McLean, I. D., & NG, K. H. (2014). Diagnostic Radiology Physics. *Tp1*, 259–261.

Devic, S., Seuntjens, J., Sham, E., Podgorsak, E. B., Schmidtlein, C. R., & Kirov, A. S. & Soares, C. G. (2005). Precise radiochromic film dosimetry using a flat-bed document scanner. *Medical Physics*, *32*(7), 2245–2253.

Edwards, C. R., Green, S., Palethorpe, J. E. & Mountford, P. J. (1997). The response of a MOSFET, p-type semiconductor and LiF TLD to quasimonoenergetic x-rays. *Physics in* Medicine and Biology, 42(12).

Ezzell G. A, Jay W. Burmeister, Nesrin Dogan, Thomas J. Losasso & James G. Mechalakos (2009). "IMRT commissioning: multiple institution planning and dosimetry comparisons, a report from AAPM Task Group 119. *Med Phys*, *36*(11), 5359–5373.

Franken, E. M., De Boer, J. C. J., Barnhoorn, J. C. & Heijmen, B. J. M. (2004). Characteristics relevant to portal dosimetry of a cooled CCD camerabased EPID. *Medical Physics*, *31*(9), 2549–2551.

Greer, P. B. (2013). 3D EPID based dosimetry for pre-treatment verification of VMAT - Methods and challenges. *Journal of Physics: Conference Series*, *444*(1). https://doi.org/10.1088/1742-6596/444/1/012010

Harari, P. M., Song, S., and Tomé, W. A. (2010). Emphasizing conformal avoidance versus target definition for IMRT planning in head-and-neck cancer.

International Journal of Radiation Oncology Biology Physics, *77*(3), 950–8.

Herman M. G, Balter JM, Jaffray DA, McGee KP, Munro P & Shalev S. (2001). Clinical use of electronic portal imaging: Report of AAPM radiation therapy committee Task Group 58. *Medical Physics*, *28*(5), 712–737.

IAEA. (2000). Absorbed dose determination in external beam radiotherapy. An international code of practice for dosimetry based on standards of absorbed dose to water. Vienna, Austria: International Atomic Energy Agency, IAEA. *IAEA Techcnical Report Series*, (398).

IAEA. (2005). *Radiation Oncology Physics : A Handbook for Teachers and Students*. (E. B. Podgorsak, Ed.). vienna.

Jaffray, D. A. (2005). Emergent technologies for 3-dimensional image-guided radiation delivery. *Seminars in Radiation Oncology*, *15*(3), :208–16.

Jin, X., Hu, W., Shang, H., Han, C., Yi, J., Zhou, Y., and Xie, C. (2013). CBCT-based volumetric and dosimetric variation evaluation of volumetric modulated arc radiotherapy in the treatment of nasopharyngeal cancer patients. *Radiation Oncology*, *8*(1), 279.

Jormet M, Ribas B & Eudaldo T. (1996). Calibration of semiconductor detectors for dose assessement in total body irradiation. *Radiother Oncol*, *38*, 247–251.

Jornet, N., Carrasco, P., Jurado, D., Ruiz, A., Eudaldo, T. & Ribas, M. (2004). Comparison study of MOSFET detectors and diodes for entrance in vivo dosimetry in 18 MV X-ray beams. *Medical Physics, 31*(9), 2534–2542.

Jursinic, P. A. (2010). Changes in optically stimulated luminescent dosimeter (OSLD)

dosimetric characteristics with accumulated dose. *Medical Physics, 37*(1), 132–140.

Karlsson, M., Ahnesjö, A., Georg, D., Nyholm, T., & Olofsson, J. (2010). Independent dose Caculations Concepts and Models. *Estro Booklet No 910*, 104.

Kaur Dhanesar, S. (2013). *The role of Cobalt-60 source in intensity modulated radioation therapy: from modeling finit sources to treatment planning and conformal dose delivery*.

Kavuma A, Glegg M, Currie G & Elliott A. (2008). Assessment of dosimetrical performance in 11 Varian a-Si-500 electronic portal imaging devices. *Physics in Medicine and Biology*, *53*(23), 6893–6909.

Kerns, J. R., Kry, S. F., Sahoo, N., Followill, D. S. & Ibbott, G. S. (2011). Angular dependence of the nanoDot OSL dosimeter. *Medical Physics*, *38*(7), 3955–3962.

Khan, F. M. (2010). *The Physics of Radiation Therapy*. (L. W. and Wilkins, Ed.) (4th ed.). Philadelphia, USA,.

Kirkby, C. & Sloboda, R. (2005). Consequences of the spectral response of an a-Si EPID and implications for dosimetric calibration. *Medical Physics*, *32*(8), 2649–2658.

Leah N. Mcdermott, B.A./B.Sc.(Hons), Markus Wendling, Ph.D., Jan-Jakob Sonke, Ph.D., Marcel Van Herk, Ph.D., And Ben J. Mijnheer, Ph.D. (2007). Replacing Pretreatment Verification With In Vivo Epid Dosimetry For Prostate Imrt, 67(5), 1568–1577. https://doi.org/10.1016/j.ijrobp.2006.11.047

Leite FMC; Ferreira FM; Cruz MSA; Lima EFA; Primo CC. Diagnósticos de

enfermagem relacionados aos efeitos adversos da radioterapia. Rev. Min. Enferm.
2013;17(4):940-5.

Meertens, H, van Herk,M & Weeda J. (1985). A liquid ionisation detector for digital radiography of therapeutic megavoltage photon beams. *Physics in Medicine and Biology*, *30*(4), 313–321.

Mijnheer, B., Beddar, S., Izewska, J. & Reft, C. (2013). In vivo dosimetry in external beam radiotherapy. *Medical Physics*, *40*(7). https://doi.org/0709031-07090319.

Muren, L. P. and Thwaites, D. I. (2013). The on-going quest for treatment precision and conformality in radiotherapy. *Radiotherapy and Oncology*, *109*(3), 337–41.

Mutic, S. and Dempsey, J. F. (2014). The ViewRay system: magnetic resonance-guided and controlled radiotherapy. *Seminars in Radiation Oncology*, *24*(3), 196–9.

Niroomand-Rad, A., Blackwell, C. R., Coursey, B. M., Gall, K. P., Galvin, J., M., Mclaughlin, W. L., Meigooni, A. S., Nath, R., Rodgers, J. E. & Soares, C., & G. (1998). Radiochromic film dosimetry: Recommendations of AAPM radiation therapy committee Task Group 55. *Medical Physics*, *25*(11), 2093–2115.

Olch, A. J. (2005). Evaluation of a computed radiography system for megavoltage photon beam dosimetry. *Medical Physics*, *32*(9), 2987–2999. https://doi.org/10.1118/1.2012787

Olch A. J, Gerig L, Li H, Mihaylov I & Morgan A. (2014). Dosimetric effects caused by couch tops and immobilization devices: report of AAPM Task Group 176. *Medical Physics, 41*(6), 061501.

Partridge, M., Philip M. Evans and Symonds-Tayler, J Richard N (1999). Optical scattering in camera-based electronic portal imaging. *Physics in Medicine and Biology*, *44*(10), 2381–2396.

Pasma, K. L., Kroonwijk, M., De Boer, J. C. J., Visser, A. G. & Heijmen, B., & M., J. (1998). Accurate portal dose measurement with a fluoroscopic electronic portal imaging device (EPID) for open and wedged beams and dynamic multileaf collimation. *Physics in Medicine and Biology*, *48*(8), 2047–2060.

Reft, C. S. (2009). The energy dependence and dose response of a commercial optically stimulated luminescent detector for kilovoltage photon, megavoltage photon, and electron, proton, and carbon beams. *Medical Physics*, *36*(5), 1690–1699.

Rührnschopf, E.-P. and Klingenbeck, K. (2011). A general framework and review of scatter correction methods in x-ray cone-beam computerized tomography. Part 1: Scatter compensation approaches. *Medical Physics*, *38*(7), 4296–4311.

Tan, Y. I. (2016). 2D transit dosimetry using electronic portal imaging device, 229. https://doi.org/glathesis:2016-7043

Van Esch, A., Depuydt T., Huyskens DP. (2004). The use of an aSi-based EPID for routine absolute dosimetric pre-treatment verification of dynamic IMRT fields. *Radiotherapy and Oncology*, *71*(2), 223–234.

Van Herk, M. (1991). Physical aspects of a liquid-filled ionization chamber with pulsed polarizing voltage. *Medical Physics*, *18*(4), 692–702.

Yukihara, E. G., Mardirossian, G., Mirzasadeghi, M., Guduru, S. & Ahmad, S. (2008). Evaluation of Al2O3: C optically stimulated luminescence (OSL)

dosimeters for passive dosimetry of high-energy photon and electron beams in radiotherapy. *Medical Physics, 35*(1), 260–269.

Zhu, Y., Jiang, X. Q. & Van Dyk, J. (1995). Portal dosimetry using a liquid ion chamber matrix: Dose response studies. *Medical Physics, 22*(7), 1101–1106.

APPENDIX

APPENDIX A: Temperature and pressure corrected ion chamber measurements used in couch TF determination

APPENDIX A1: Measurements at gantry angle 180°

At depth of 20cm

Temperature = 24.1°C Pressure = kPa 98.85 Humidity = 22 % kcor=1.039372

FIELD SIZE (cm^2)	Readings (nC)					Mean Readings (nC)	Mcor=Kcor*mean reading
	1	2	3	4	5		
10 x 10	0.559	0.561	0.562	0.563	0.563	0.5616	0.583711
4 x 4	0.057	0.057	0.057	0.057	0.057	0.057	0.059244
5 x 5	0.146	0.146	0.146	0.146	0.146	0.146	0.151748
6 x 6	0.290	0.290	0.290	0.290	0.291	0.2902	0.301626
8 x 8	0.486	0.485	0.486	0.486	0.486	0.4858	0.504927
10 x 10	0.554	0.554	0.554	0.555	0.554	0.5542	0.57602
15 x 15	0.658	0.659	0.660	0.660	0.660	0.6594	0.685362
20 x 20	0.731	0.731	0.731	0.731	0.731	0.731	0.759781
25 x 25	0.782	0.782	0.783	0.783	0.783	0.7826	0.813413
30 x 30	0.812	0.812	0.813	0.812	0.812	0.8122	0.844178
10 x 10	0.555	0.555	0.555	0.555	0.555	0.555	0.576851
32 x 32	0.818	0.819	0.819	0.818	0.819	0.8186	0.85083
10 x 10	0.555	0.555	0.555	0.555	0.555	0.555	0.576851

APPENDIX A2: Depth of 15cm

Temperature = 23.8 °C Pressure = 98.86 kPa Humidity = 23 % kcor=1.038218

FIELD SIZE (cm^2)	Readings (nC)					Mean Readings (nC)	Mcor=Kcor*mean reading
	1	2	3	4	5		
10 x 10	0.862	0.862	0.863	0.863	0.863	0.8626	0.895567
4 x 4	0.142	0.143	0.143	0.143	0.143	0.1428	0.148258
5 x 5	0.401	0.403	0.403	0.403	0.403	0.4026	0.417987
6 x 6	0.604	0.604	0.604	0.604	0.604	0.604	0.627084
8 x 8	0.808	0.809	0.808	0.808	0.808	0.8082	0.839088
10 x 10	0.876	0.876	0.876	0.876	0.876	0.876	0.909479
15 x 15	1.001	1.001	1.002	1.002	1.002	1.0016	1.039879
20 x 20	1.105	1.106	1.105	1.105	1.105	1.1052	1.147439
25 x 25	1.160	1.160	1.160	1.160	1.160	1.160	1.204333
30 x 30	1.190	1.190	1.190	1.190	1.190	1.190	1.235479
10 x 10	0.876	0.876	0.876	0.876	0.876	0.876	0.909479
32 x 32	1.194	1.195	1.195	1.195	1.195	1.1948	1.240463
10 x 10	0.876	0.876	0.876	0.876	0.876	0.876	0.909479

APPENDIX A3: DEPTH OF 10cm

Temperature = 23.8 °C Pressure = 97.80 kPa Humidity = 23 % kcor= 1.0492166586

FIELD SIZE (cm^2)	Readings (nC)					Mean Readings (nC)	Mcor=Kcor *mean reading
	1	2	3	4	5		
10 x 10	1.253	1.256	1.256	1.256	1.256	1.2554	1.317187
4 x 4	0.936	0.936	0.93	0.93	0.93	0.9324	0.97829
5 x 5	1.039	1.039	1.03	1.03	1.03	1.0336	1.08447
6 x 6	1.085	1.086	1.086	1.085	1.086	1.0856	1.13903
8 x 8	1.61	1.612	1.612	1.612	1.612	1.6116	1.690918
10 x 10	1.234	1.234	1.234	1.234	1.234	1.234	1.294733
15 x 15	1.358	1.358	1.358	1358	1.358	272.6864	286.1071
20 x 20	1.447	1.447	1.448	1.448	1.447	1.4474	1.518636
25 x 25	1.509	1.509	1.509	1.509	1.509	1.509	1.583268
30 x 30	1.543	1.544	1.544	1.554	1.544	1.5458	1.621879
10 x 10	1.232	1.233	1.233	1.223	1223	245.5842	257.671
32 x 32	1.551	1.551	1.551	1.552	1.551	1.5512	1.627545
10 x 10	1.234	1.234	1.234	1.234	1.234	1.234	1.294733

APPENDIX A4: Depth of 5 cm

Temperature = 23.3 °C Pressure = 97.77 kPa Humidity = 23 % Kcor = 1.047768617

FIELD SIZE (cm^2)	Readings (nC)					Mean Readings (nC)	Mcor=Kcor *mean reading
10 x 10	1.672	1.672	1.672	1.672	1.672	1.672	1.751869
4 x 4	0.766	0.766	0.765	0.765	0.766	0.7656	0.802172
5 x 5	1.448	1.447	1.447	1.447	1.447	1.4472	1.516331
6 x 6	1.539	1.539	1.539	1.538	1.539	1.5388	1.612306
8 x 8	1.628	1.629	1.629	1.629	1.629	1.6288	1.706605
10 x 10	1.698	1.698	1.698	1.698	1.698	1.698	1.779111
15 x 15	1.834	1.834	1.833	1.834	1.834	1.8338	1.921398
20 x 20	1.926	1.925	1.925	1.926	1.926	1.9256	2.017583
25 x 25	1.987	1.987	1.986	1.987	1.876	1.9646	2.058446
30 x 30	2.022	2.023	2.022	2.022	2.022	2.0222	2.118798
10 x 10	1.702	1.702	1.702	1.702	1.702	1.702	1.783302
32 x 32	2.029	2.030	2.030	2.030	2.030	2.0298	2.126761
10 x 10	1.700	1.700	1.700	1.700	1.700	1.7	1.781207

APPENDIX A5: Depth of 0 cm

Temperature = 23.3 °C Pressure = 97.79 kPa Humidity = 23 % Kcor = 1.0475543277

FIELD SIZE (cm^2)	Readings (nC)					Mean Readings (nC)	Mcor=Kcor* mean reading
	1	2	3	4	5		
10 x 10	2.157	2.157	2.158	2.157	2.157	2.1572	2.259775
4 x 4	1.078	1.079	1.078	1.078	1.078	1.0782	1.129468
5 x 5	1.815	1.815	1.816	1.815	1.815	1.8152	1.901513
6 x 6	2.107	2.107	2.107	2.107	2.107	2.107	2.207188
8 x 8	2.174	2.175	2.174	2.174	2.174	2.1742	2.277583
10 x 10	2.231	2.231	2.231	2.231	2.231	2.231	2.337084
15 x 15	2.351	2.350	2.351	2.352	2.352	2.3512	2.463
20 x 20	2.436	2.435	2.436	2.436	2.435	2.4356	2.551413
25 x 25	2.496	2.496	2.496	2.496	2.496	2.496	2.614685
30 x 30	2.526	2.526	2.525	2.526	2.526	2.5258	2.645902
10 x 10	2.232	2.232	2.232	2.233	2.232	2.2322	2.338341
32 x 32	2.536	2.535	2.535	2.535	2.535	2.5352	2.655749
10 x 10	2.237	2.237	2.237	2.237	2.237	2.237	2.343369

APPENDIX B: Corrected ion chamber measurements at angle 0o
APPENDIX B1: Depth of 5 cm

Temperature = 23.3 °C Pressure = 97.62 kPa Humidity = 23 %
Kcor=1.049636

FIELD SIZE (cm^2)	Readings (nC)					Mean Readings (nC)	Mcor=Kcor*mean reading
	1	2	3	4	5		
10 x 10	1.677	1.677	1.678	1.678	1.678	1.6776	1.760869
4 x 4	1.453	1.453	1.452	1.453	1.453	1.4528	1.524911
5 x 5	1.505	1.505	1.506	1.506	1.505	1.5054	1.580122
6 x 6	1.558	1.558	1.558	1.558	1.558	1.558	1.635333
8 x 8	1.616	1.615	1.616	1.615	1.615	1.6154	1.695582
10 x 10	1.678	1.677	1.678	1.678	1.678	1.6778	1.761079
15 x 15	1.800	1.799	1.799	1.799	1.799	1.7992	1.888505
20 x 20	1.892	1.892	1.892	1.892	1.892	1.892	1.985911
25 x 25	1.957	1.956	1.957	1.957	1.957	1.9568	2.053928
30 x 30	1.987	1.987	1.987	1.987	1.987	1.987	2.085627
10 x 10	1.672	1.672	1.672	1.672	1.671	1.6718	1.754781
32 x 32	1.995	1.995	1.995	1.995	1.995	1.995	2.094024
10 x 10	1.665	1.665	1.663	1.665	1.665	1.6646	1.747224

APPENDIX B2: Depth of 0 cm (076).

Temperature = 23.4 °C Pressure = 97.65 kPa Humidity = 23 %
Kcor=1.049667

FIELD SIZE (cm^2)	Readings (nC)					Mean Readings (nC)	Mcor=Kcor*mean reading
	1	2	3	4	5		
10 x 10	1.734	1.735	1.735	1.735	1.735	1.735	1.821172
4 x 4	1.457	1.458	1.458	1.459	1.459	1.4582	1.530624
5 x 5	1.508	1.508	1.508	1.509	1.509	1.5084	1.583318
6 x 6	1.563	1.563	1.564	1.565	1.564	1.5638	1.641469
8 x 8	1.666	1.666	1.667	1.667	1.668	1.6668	1.749585
10 x 10	1.767	1.767	1.768	1.767	1.768	1.7674	1.855181
15 x 15	1.987	1.987	1.988	1.988	1.988	1.9876	2.086318
20 x 20	2.208	2.208	2.209	2.208	2.209	2.2084	2.318085
25 x 25	2.408	2.408	2.407	2.409	2.409	2.4082	2.527808
30 x 30	2.576	2.577	2.577	2.577	2.576	2.5766	2.704572
10 x 10	1.743	1.743	1.742	1.743	1.743	1.7428	1.82936
32 x 32	2.679	2.679	2.680	2.680	2.680	2.6796	2.812688
10 x 10	1.798	1.798	1.799	1.799	1.7999	1.79878	1.88812

APPENDIX B3: Depth of 20 cm (1576).

Temperature = 23.3 °C Pressure = 97.86 kPa Humidity = 24 % Kcor=1.047061

FIELD SIZE (cm^2)	Readings (nC)					Mean Readings (nC)	Mcor=Kcor *mean reading
	1	2	3	4	5		
10 x 10	0.565	0.563	0.561	0.561	0.560	0.562	0.588723
4 x 4	0.409	0.410	0.409	0.409	0.409	0.4092	0.428657
5 x 5	0.438	0.437	0.437	0.436	0.435	0.4366	0.45736
6 x 6	0.464	0.464	0.464	0.463	0.463	0.4636	0.485644
8 x 8	0.506	0.505	0.504	0.504	0.504	0.5046	0.528594
10 x 10	0.547	0.546	0.546	0.545	0.545	0.5458	0.571753
15 x 15	0.633	0.633	0.633	0.633	0.633	0.633	0.663099
20 x 20	0.695	0.695	0.695	0.695	0.695	0.695	0.728047
25 x 25	0.742	0.742	0.742	0.742	0.742	0.742	0.777282
30 x 30	0.771	0.771	0.771	0.771	0.770	0.7708	0.807452
10 x 10	0.540	0.540	0.540	0.540	0.540	0.54	0.565677
32 x 32	0.777	0.777	0.777	0.777	0.777	0.777	0.813946
10 x 10	0.539	0.540	0.539	0.540	0.539	0.5394	0.565048

APPENDIX B4: Depth of 15 cm .

Temperature = 23.1 °C Pressure = 97.57 kPa Humidity = 24 %
Kcor=1.049465

FIELD SIZE (cm^2)	Readings (nC)					Mean Readings (nC)	Mcor=Kcor*mean reading
	1	2	3	4	5		
10 x 10	0.871	0.872	0.871	0.871	0.870	0.871	0.912416
4 x 4	0.671	0.671	0.671	0.670	0.669	0.6704	0.702278
5 x 5	0.712	0.712	0.712	0.711	0.712	0.7118	0.745646
6 x 6	0.750	0.751	0.750	0.751	0.750	0.7504	0.786082
8 x 8	0.816	0.815	0.815	0.815	0.815	0.8152	0.853963
10 x 10	0.868	0.867	0.867	0.867	0.867	0.8672	0.908435
15 x 15	0.979	0.978	0.979	0.979	0.979	0.9788	1.025342
20 x 20	1.059	1.059	1.059	1.059	1.059	1.059	1.109355
25 x 25	1.113	1.113	1.113	1.113	1.113	1.113	1.165923
30 x 30	1.146	1.146	1.145	1.144	1.144	1.145	1.199445
10 x 10	0.862	0.862	0.862	0.861	0.862	0.8618	0.902779
32 x 32	1..150	1.150	1.150	1.150	1.150	1.15	1.204683
10 x 10	0.863	0.863	0.863	0.862	0.862	0.8626	0.903617

APPENDIX B5: Depth of 10 cm (576).

Temperature = C22.8 Pressure =97.57 kPa Humidity = 24 % Kcor=1.048403

FIELD SIZE (cm^2)	Readings (nC)					Mean Readings (nC)	Mcor=Kcor *mean reading
	1	2	3	4	5		
10 x 10	0.911	1.204	1.204	1.204	1.204	1.1454	1.199864
4 x 4	0.961	0.960	0.961	0.960	0.960	0.9604	1.006067
5 x 5	1.022	1.021	1.022	1.022	1.022	1.0218	1.070387
6 x 6	1.066	1.066	1.066	1.066	1.066	1.066	1.116688
8 x 8	1.124	1.137	1.137	1.137	1.137	1.1344	1.188341
10 x 10	1.197	1.196	1.196	1.197	1.197	1.1966	1.253498
15 x 15	1.323	1.323	1.323	1.323	1.322	1.3228	1.385699
20 x 20	1.409	1.409	1.408	1.408	1.408	1.4084	1.475369
25 x 25	1.468	1.468	1.467	1.468	1.468	1.4678	1.537594
30 x 30	1.503	1.503	0.503	1.503	1.503	1.303	1.364958
10 x 10	1.177	1.178	1.178	1.178	1.178	1.1778	1.233804
32 x 32	1.483	1.508	1.506	1.508	1.508	1.5026	1.574049
10 x 10	1.175	1.176	1.176	1.176	1.177	1.176	1.231919

APPENDIX C: Couch transmission factors at the various depths

Field size	Couch transmission factor for 0° & 180° angles				
	Depth				
	0cm	5cm	10cm	15cm	20cm
4x4	0.739840091	0.527415698	0.147244077	0.210725154	0.038850792
5x5	1.204102398	0.962129506	0.390183317	0.559547475	0.096035623
6x6	1.348152173	0.988488583	0.561099787	0.796277931	0.184443168
8x8	1.305183801	1.009124301	0.705526239	0.980788382	0.297789785
10x10	1.262925572	1.011101915	0.73349136	0.983653513	0.328651801
15x15	1.183630683	1.020068785	0.749826042	1.012327495	0.362912463
20x20	1.103528991	1.018596	0.777097072	1.032442461	0.382585624
25x25	1.037068875	1.004811269	0.782620873	1.031058469	0.396028001
30x30	0.980861297	1.018551735	0.788904536	1.028163247	0.404759816
32x32	0.946668454	1.018280115	0.78743057	1.027822038	0.406313395

APPENDIX D: Raw diode calibration measurements

APPENDIX D1

Depth=0.5cm						
Field size(cm^2)	Ion chamber Readings (nC)			Mean (nC)	$K_{T,P}$ corrected	Dose (cGy)
	1	2	3			
5x5	2.089	2.088	2.089	2.088667	2.185955	64.59497
6x6	2.123	2.123	2.122	2.122667	2.221539	65.64646
8x8	2.178	2.177	2.178	2.177667	2.2791	67.34742
10x10	2.228	2.228	2.229	2.228333	2.332127	68.91435
12x12	2.277	2.278	2.277	2.277333	2.383409	70.42975
15x15	2.339	2.339	2.338	2.338667	2.4476	72.32657
20x20	2.415	2.415	2.416	2.415333	2.527837	74.69759
25x25	2.469	2.468	2.469	2.468667	2.583655	76.347
10x10	2.229	2.228	2.229	2.228667	2.332476	68.92466
30x30	2.497	2.498	2.497	2.497333	2.613657	77.23356

APPENDIX D2

Depth=1.5cm						
Field size(cm^2)	Ion chamber Readings (nC)			Mean (nC)	$K_{T,P}$ corrected	Dose (cGy)
	1	2	3			
5x5	1.999	1.998	1.999	1.998667	2.091763	61.81159
6x6	2.033	2.034	2.033	2.033333	2.128044	62.8837
8x8	2.090	2.091	2.090	2.090333	2.187699	64.64651
10x10	2.138	2.138	2.137	2.137667	2.237237	66.11036
12x12	2.181	2.181	2.180	2.180667	2.28224	67.4402
15x15	2.242	2.241	2.242	2.241667	2.346081	69.32671
20x20	2.317	2.318	2.317	2.317333	2.425273	71.66681
25x25	2.360	2.360	2.361	2.360333	2.470276	72.99664
10x10	2.140	2.140	2.139	2.139667	2.23933	66.17221
30x30	2.380	2.381	2.380	2.380333	2.491207	73.61517

APPENDIX D3

Depth=2.5cm						
Field size(cm^2)	Ion chamber Readings (nC)			Mean (nC)	$K_{T,P}$ corrected	Dose (cGy)
	1	2	3			
5x5	1.863	1.862	1.863	1.862667	1.949428	57.6056
6x6	1.910	1.911	1.910	1.910333	1.999315	59.07976
8x8	1.969	1.970	1.969	1.969333	2.061063	60.90441
10x10	2.020	2.021	2.020	2.020333	2.114439	62.48166
12x12	2.066	2.065	2.066	2.065667	2.161884	63.88366
15x15	2.127	2.127	2.128	2.127333	2.226423	65.79079
20x20	2.201	2.200	2.201	2.200667	2.303172	68.05872
25x25	2.249	2.250	2.249	2.249333	2.354105	69.56381
10x10	2.018	2.019	2.019	2.018667	2.112694	62.43012
30x30	2.270	2.269	2.270	2.269667	2.375386	70.19265

APPENDIX D4

Depth=3.5cm						
Field size(cm^2)	Ion chamber Readings (nC)			Mean (nC)	$K_{T,P}$ corrected	Dose (cGy)
	1	2	3			
5x5	1.725	1.724	1.725	1.724667	1.805	53.33775
6x6	1.778	1.777	1.778	1.777667	1.860469	54.97685
8x8	1.843	1.844	1.843	1.843333	1.929194	57.00769
10x10	1.893	1.893	1.894	1.893333	1.981523	58.55401
12x12	1.944	1.945	1.945	1.944667	2.035247	60.14156
15x15	2.007	2.008	2.007	2.007333	2.100833	62.07962
20x20	2.080	2.081	2.080	2.080333	2.177233	64.33725

25x25	2.127	2.128	2.127	2.127333	2.226423	65.79079
10x10	1.896	1.895	1.896	1.895667	1.983965	58.62617
30x30	2.150	2.151	2.150	2.150333	2.250494	66.50209

APPENDIX D5

Depth=10.5cm						
Field size(cm^2)	Ion chamber Readings (nC)			Mean (nC)	$K_{T,P}$ corrected	Dose (cGy)
	1	2	3			
5x5	0.950	0.951	0.950	0.950333	0.994599	29.3904
6x6	1.005	1.004	1.005	1.004667	1.051463	31.07074
8x8	1.074	1.074	1.075	1.074333	1.124375	33.22528
10x10	1.134	1.135	1.134	1.134333	1.18717	35.08086
12x12	1.187	1.187	1.188	1.187333	1.242638	36.71996
15x15	1.248	1.249	1.248	1.248333	1.30648	38.60647
20x20	1.320	1.321	1.320	1.320333	1.381833	40.83317
25x25	1.364	1.365	1.364	1.364333	1.427883	42.19393
10x10	1.131	1.130	1.131	1.130667	1.183332	34.96746
30x30	1.382	1.381	1.382	1.381667	1.446023	42.72999

APPENDIX D6

Depth=12.5cm						
Field size(cm^2)	Ion chamber Readings (nC)			Mean (nC)	$K_{T,P}$ corrected	Dose (cGy)
	1	2	3			
5x5	0.797	0.798	0.797	0.797333	0.834472	24.65866
6x6	0.843	0.844	0.843	0.843333	0.882615	26.08127
8x8	0.909	0.909	0.908	0.908667	0.950992	28.1018
10x10	0.960	0.960	0.961	0.960333	1.005065	29.69966
12x12	1.015	1.016	1.015	1.015333	1.062627	31.40062
15x15	1.074	1.075	1.074	1.074333	1.124375	33.22528
20x20	1.144	1.145	1.144	1.144333	1.197635	35.39012
25x25	1.185	1.186	1.185	1.185333	1.240545	36.65811
10x10	0.958	0.959	0.959	0.958667	1.00332	29.64812
30x30	1.202	1.202	1.203	1.202333	1.258337	37.18386

APPENDIX D7

Depth=15.5cm						
Field size(cm^2)	Ion chamber Readings (nC)			Mean (nC)	$K_{T,P}$ corrected	Dose (cGy)
	1	2	3			
5x5	0.600	0.601	0.601	0.600667	0.628645	18.57646
6x6	0.642	0.643	0.642	0.642333	0.672253	19.86507

8x8	0.700	0.700	0.701	0.700333	0.732954	21.6588
10x10	0.747	0.746	0.747	0.746667	0.781446	23.09172
12x12	0.792	0.793	0.792	0.792333	0.829239	24.50403
15x15	0.847	0.847	0.848	0.847333	0.886801	26.20498
20x20	0.908	0.909	0.908	0.908333	0.950643	28.09149
25x25	0.949	0.949	0.950	0.949333	0.993552	29.35947
10x10	0.747	0.747	0.748	0.747333	0.782143	23.11234
30x30	0.965	0.966	0.965	0.965333	1.010298	29.8543

APPENDIX E: Raw Diode readings for diode calibration

APPENDIX E1

Field size(cm^2)	Diode Readings (nC)			Mean (nC)
	1	2	3	
5x5	49.63	49.59	49.58	49.6
6x6	50.20	50.20	50.21	50.20333
8x8	51.79	51.78	51.79	51.78667
10x10	52.95	52.96	52.95	52.95333
12x12	54.11	54.11	54.10	54.10667
15x15	55.58	55.57	55.58	55.57667
20x20	57.44	57.44	57.45	57.44333
25x25	58.69	58.69	58.70	58.69333
10x10	53.17	53.16	53.17	53.16667
30x30	59.37	59.36	59.37	59.36667

APPENDIX E2

Field size(cm^2)	Diode Readings (nC)			Mean (nC)
	1	2	3	
5x5	45.30	45.31	45.30	45.30333
6x6	46.54	46.54	46.55	46.54333
8x8	47.96	47.97	47.96	47.96333
10x10	49.25	49.26	49.26	49.25667
12x12	50.43	50.44	50.43	50.43333
15x15	51.92	51.94	51.92	51.92667
20x20	53.93	53.94	53.93	53.93333
25x25	55.22	55.23	55.23	55.22667
10x10	49.24	49.24	49.25	49.24333
30x30	55.95	55.95	55.94	55.94667

APPENDIX E3

Field size(cm^2)	Diode Readings (nC)			Mean (nC)
	1	2	3	
5x5	42.49	42.50	49.49	44.82667
6x6	43.64	43.64	43.65	43.64333
8x8	45.14	45.15	45.14	45.14333
10x10	46.62	46.62	46.63	46.62333
12x12	47.80	47.81	47.80	47.80333
15x15	49.42	49.42	49.41	49.41667
20x20	51.47	51.47	51.47	51.47
25x25	52.82	52.82	52.83	52.82333
10x10	46.52	46.52	46.51	46.51667
30x30	53.62	53.63	53.62	53.62333

APPENDIX E4

Field size(cm^2)	Diode Readings (nC)			Mean (nC)
	1	2	3	
5x5	39.15	39.14	39.15	39.14667
6x6	40.71	40.72	40.71	40.71333
8x8	42.43	42.44	42.43	42.43333
10x10	43.89	43.90	43.90	43.89667
12x12	45.20	45.20	45.21	45.20333
15x15	46.84	46.85	46.84	46.84333
20x20	48.95	48.96	48.95	48.95333
25x25	50.38	50.38	50.37	50.37667
10x10	43.79	43.80	43.80	43.79667
30x30	51.13	51.14	51.14	51.13667

APPENDIX E5

Field size(cm^2)	Diode Readings (nC)			Mean (nC)
	1	2	3	
5x5	21.62	21.63	21.62	21.62333
6x6	22.97	22.98	22.97	22.97333
8x8	24.86	24.86	24.85	24.85667
10x10	26.57	26.57	26.56	26.56667
12x12	28.04	28.05	28.04	28.04333
15x15	29.84	29.84	29.85	29.84333
20x20	32.17	32.17	32.18	32.17333
25x25	33.77	33.78	33.77	33.77333
10x10	26.48	26.48	26.49	26.48333
30x30	34.64	34.65	34.64	34.64333

APPENDIX E6

Field size(cm^2)	Diode Readings (nC)			Mean (nC)
	1	2	3	
5x5	18.17	18.17	18.16	18.16667
6x6	19.32	19.33	19.33	19.32667
8x8	21.06	21.07	21.06	21.06333
10x10	22.64	22.64	22.64	22.64
12x12	24.02	24.03	24.02	24.02333
15x15	25.84	25.84	25.84	25.84
20x20	28.12	28.13	28.12	28.12333
25x25	29.68	29.69	29.70	29.69
10x10	22.88	22.87	22.87	22.87333
30x30	30.52	30.53	30.52	30.52333
Field size(cm^2)	Diode Readings (nC)			Mean (nC)
	1	2	3	
5x5	13.93	13.94	13.94	13.93667
6x6	14.86	14.86	14.85	14.85667
8x8	16.43	16.44	16.43	16.43333
10x10	17.82	17.82	17.82	17.82
12x12	19.10	19.10	19.11	19.10333
15x15	20.75	20.76	20.75	20.75333
20x20	22.87	22.88	22.88	22.87667
25x25	24.38	24.39	24.38	24.38333
10x10	17.71	17.71	17.72	17.71333
30x30	25.14	25.15	25.14	25.14333

APPENDIX F: Exit dose measurements

APPENDIX F1

Field size (cm^2)	Ion chamber reading at slab depth of 7cm (nC)			Mean (nC)	$K_{T,P}$ & TF_c corrected (nC)	Dose (cGy)
	1	2	3			
5x5	2.291	2.290	2.291	2.290667	2.471509	73.03309
7x7	2.247	2.246	2.246	2.246333	2.423676	71.61962
10x10	2.180	2.180	2.181	2.180333	2.352465	69.51535
12x12	2.158	2.158	2.158	2.158	2.328369	68.8033
15x15	2.119	2.119	2.118	2.118667	2.28593	67.54924
DEPTH OF 10cm						
5x5	2.122	2.123	2.122	2.122333	2.289886	67.66614
7x7	2.049	2.050	2.049	2.049333	2.211123	65.33869
10x10	1.968	1.968	1.969	1.968333	2.123728	62.75617
12x12	1.934	1.934	1.933	1.933667	2.086325	61.6509
15x15	1.891	1.892	1.891	1.891333	2.040649	60.30119
Depth of 12cm						

5x5	1.938	1.939	1.938	1.938333	2.09136	61.79969
7x7	1.881	1.881	1.881	1.881	2.0295	59.97173
10x10	1.788	1.789	1.788	1.788333	1.929518	57.01725
12x12	1.739	1.739	1.740	1.739333	1.876649	55.45499
15x15	1.692	1.692	1.691	1.691667	1.82522	53.93524
Depth of 15cm						
5x5	1.768	1.769	1.768	1.768333	1.907939	56.37959
7x7	1.695	1.695	1.695	1.695	1.828816	54.04151
10x10	1.593	1.593	1.594	1.593333	1.719123	50.80009
12x12	1.540	1.540	1.541	1.540333	1.661939	49.11029
15x15	1.482	1.482	1.481	1.481667	1.598641	47.23983

APPENDIX F2

Field size (cm^2)	Ion chamber readings for 7cm in anthropomorphic phantom (nC)			Mean (nC)	TF_C, F_{cal} & CF_{fs} corrected (nC)	Dose (cGy)
	1	2	3			
5x5	0.857	0.857	0.858	0.857333	0.925018	27.33427
7x7	0.841	0.842	0.841	0.841333	0.907755	26.82415
10x10	0.835	0.836	0.835	0.835333	0.901281	26.63285
12x12	0.837	0.837	0.838	0.837333	0.903439	26.69661
15x15	0.841	0.841	0.842	0.841333	0.907755	26.82415
DEPTH OF 10cm						
5x5	1.021	1.021	1.020	1.020667	1.101246	32.54181
7x7	0.997	0.997	0.998	0.997333	1.07607	31.79788
10x10	0.970	0.971	0.970	0.970333	1.046939	30.93704
12x12	0.961	0.961	0.961	0.961	1.036869	30.63947
15x15	0.957	0.957	0.958	0.957333	1.032912	30.52256
Depth of 12cm						
5x5	1.146	1.146	1.147	1.146333	1.236833	36.54843
7x7	1.125	1.125	1.124	1.124667	1.213456	35.85763
10x10	1.081	1.080	1.081	1.080667	1.165983	34.45479
12x12	1.062	1.061	1.062	1.061667	1.145483	33.84901
15x15	1.050	1.051	1.050	1.050333	1.133255	33.48767
Depth of 15cm						
5x5	1.378	1.379	1.378	1.378333	1.487149	43.94526
7x7	1.332	1.333	1.332	1.332333	1.437518	42.47865
10x10	1.272	1.273	1.272	1.272333	1.372781	40.56568
12x12	1.238	1.238	1.238	1.238	1.335737	39.47103
15x15	1.214	1.214	1.213	1.213667	1.309483	38.69521

APPENDIX F3

FIELD SIZE	BARRACUDA Dose at 7cm in Anthropomorphic Phantom (mGy)		Mean Dose (mGy)	Corrected for couch factor (cGy)
	1	2		
5x5	98.96	98.87	98.915	27.63427
7x7	95.03	94.72	94.875	26.82415
10x10	97.16	97.03	97.095	26.73285
12x12	99.27	99.2	99.235	26.69661
15x15	99.36	99.28	99.32	26.52415
Depth of 10cm				
5x5	85.65	85.33	85.49	32.54181
7x7	83.24	83.05	83.145	31.69788
10x10	84.24	84.5	84.37	30.93704
12x12	85.97	85.59	85.78	30.63947
15x15	84.24	84.23	84.235	30.52256
Depth of 12cm				
5x5	82.84	82.68	82.76	36.54843
7x7	79.47	79.69	79.58	35.05763
10x10	76.06	75.69	75.875	34.45479
12x12	74.59	74.27	74.43	33.94901
15x15	73.67	73.65	73.66	33.2767
Depth of 15cm				
5x5	73.5	72.99	73.245	43.14526
7x7	69.42	69.5	69.46	42.17865
10x10	68.27	68.3	68.285	40.90568
12x12	65.33	65.4	65.365	39.5103
15x15	62.7	62.8	62.75	38.7521